MASTER'S THESIS

Development of a mesoporous ZrO_2-coating for sensing applications using ATR-FTIR spectroscopy

by Dominik Wacht, BSc

conducted at the Institute of Chemical Technologies and Analytics

at the Technische Universität Wien

in the research division Process Analytics

under the supervision of Univ.Prof. Dipl.-Ing. Dr.techn.Bernhard Lendl

by Dominik Wacht, BSc

_____ _____

Date Signature

Acknowledgements

First of all, I would like to thank Bernhard Lendl for giving me the opportunity to conduct my master's thesis in his group. His scientific input and great ideas helped me in overcoming all the obstacles I encountered during my work. Of course, I am also happy for the financial support as well as the opportunity to participate in the IRDG conference in London.

Furthermore, I would like to thank my colleagues in the research division Process Analytics for our daily trips to Billa and nice chats in the office. Special thanks goes to Felix Frank, who always managed to keep our ATR grinding sessions a musical as well as a culinary highlight of the day. Additionally, I would like to thank Stephan Freitag for showing me the ropes when I first started working in the group as an intern and Ana Catarina Vieira Dias Dos Santos for helping me with the Raman measurements.

Very special thanks goes to Werner Artner from the XRC at TU Wien. Thank you for showing me how to measure at the XRD instruments, for continuously answering all of my question and your constant cheerful mood.

I would like to thank Nuria Teigell Beneitez from IMEC at Ghent University for providing the Si- and Ge-wafer I used in my thesis. I would also like to thank Anna Zahoranova and Stefan Helfert for helping me with the contact angle measurements. Many thanks to Matthias Weil for letting me use his oven for calcination and to USTEM at TU Wien for letting me use the sample preparation lab.

I want to thank my parents Elisabeth and Gerhard Wacht, who kept morally and financially supporting me all these years. I especially enjoy our conversations and the card games we play and of course the food that you generously provide when I am visiting you. I want to thank my favourite sister Daniela Wacht, who keeps constantly calling me at the most unearthly hours and our weekly strolls in the not so uncharted territories of our home.

And finally and definitely most importantly, I would like to express my deepest appreciation and gratitude for my girlfriend Daniela Kau. I am so happy and proud that you already received your master's degrees and with distinction no less. Can you believe it's been seven and a half years when we started our studies together and seven years since we've been together? We've endured a lot of hard times, not to mention the Corona pandemic, but I can't see an obstacle we can't overcome, together.

Contents

List of figures

List of tables

Table 1: List of abbreviations and meaning

Abbreviations	Meaning
2θ	Diffraction angle
ADC	Analogue-Digital-Converter
ATR	Attenuated Total Reflection
BET	Brunauer-Emmett-Teller
d-spacing	Interplanar spacing
EISA	Evaporation Induced Self-Assembly
FTIR	Fourier Transform InfraRed
GI-SAXS	Grazing Incidence-Small Angle X-ray Scattering
hex	hexagonal
H_RH 35 %-coating	a coating from the H-solution spin coated at a RH of 35 %
H-solution	Precursor solution with the highest amount of HCl (3.6 equivalents)
IR	InfraRed
IRE	Internal Reflection Element
IRS	Internal Reflection Spectroscopy
L_RH 50 %-coating	a coating from the L-solution spin coated at a RH of 50 %
L-solution	Precursor solution with the lowest amount of HCl (2.4 equivalents)
MCT	Mercury-Cadmium-Telluride
MIR	Mid-InfraRed
PTFE	PolyTetraFluorEthylene
RH	Relative Humidity
XRD	X-Ray Diffraction

Abstract

Mesoporous silica is an extensively studied material and has been used in ATR-IR sensing schemes due to its high surface area and tuneable surface chemistry. However, the poor chemical stability in aqueous solutions at pH values higher than 8 as well as the strong absorption below 1200 cm^{-1} limits the range of applications. Therefore, a mesoporous zirconia coating was developed to circumvent these problems.

A precursor solution was deposited on Si- and Ge-ATR elements utilising the evaporation induced self-assembly process. The prepared coatings were analysed with XRD, GI-SAXS, Raman and FTIR spectroscopy to evaluate the influence of reaction, coating and ageing parameters. The film thickness and, additionally, the thermal and chemical stability of different coatings were analysed. The pristine coating was used for enrichment studies of the ionic species cetyltrimethylammonium bromide and potassium dihydrogenphosphate. The surface was then chemically modified with silanes and characterised by FTIR spectroscopy, XRD and contact angle measurements. The modified coatings were used for the enrichment of benzonitrile, valeronitrile and benzene.

Mesoporous zirconia coatings were successfully prepared and an optimised ageing process developed. Calcination of the coatings at 500°C was necessary to remove the surfactant of the precursor solution and to obtain cubic mesostructures. The mesoporous structure was still present after heating to 900°C in atmospheric conditions and after keeping the coating in aqueous solution at a pH value of 12 for 72 h. Enrichments with ionic species were successful, but not applicable for sensing schemes as the analytes could not be completely removed after enrichment. For potassium dihydrogenphosphate, enrichments with concentrations of 5 mg L^{-1} were achieved. Fast enrichments of 10 mg L^{-1} benzonitrile, 25 mg L^{-1} valeronitrile and 12 mg L^{-1} benzene were achieved as well as the complete removal of these analytes proving the applicability of these coatings for sensing applications.

Further characterisation of the mesoporous zirconia coatings and enrichments of various analytes are necessary to determine possible applications of these coatings.

1. Introduction

1.1. ATR-FTIR spectroscopy

In spectroscopy, infrared (IR) radiation can be used to excite molecular vibrations in molecules. Every vibrational mode involves the displacement of atoms from their equilibrium positions with a characteristic frequency. The energy required for transitions between the ground and the first excited state are in the mid-infrared (MIR) region of 4000 cm^{-1} to 400 cm^{-1}. For many vibrational modes, a few atoms experience large displacement, while the others remain almost stationary. These modes are characteristic for functional groups present in the molecule. Other bands involve the motion of several atoms and their frequency vary depending on the individual molecule. These modes, which are known as fingerprint bands, can be used to distinguish one molecule from the other, when both contain the same functional group. For these reasons, the vibrational modes of every single molecule is unique and can be used for identifying the specific molecule [1].

Furthermore, quantitative analysis can be performed using the Beer-Lambert law, where the absorbance can be calculated with the following equation [1, 2]:

$$A = -log_{10}\left(\frac{\Phi_t}{\Phi_0}\right) = \varepsilon * c * b \qquad \text{(Eq. 1)}$$

A…absorbance ( )

Φ_t, Φ_0… transmitted and incident radiant power (W)

ε…molar decadic absorption coefficient (L mol^{-1} cm^{-1})

c…amount concentration (mol L^{-1})

b…absorption path length (cm)

Equation 1: Beer-Lambert law. Reproduced from ref. [2].

Therefore, IR spectroscopy is a powerful tool to directly obtain qualitative and quantitative information on molecules [1, 2]. Measurements were conventionally performed in transmission configuration until internal reflection was introduced to vibrational spectroscopy by J. Fahrenfort and N. J. Harrick. The phenomenon of internal reflection was observed centuries ago, where radiation passing through a dense medium is totally reflected at the interface with a rarer medium and an energy field extends into the latter. The interest in internal reflection grew with the detailed description of basic theory, various applications and inventive apparatus. Internal reflection spectroscopy (IRS) as well as attenuated total reflection (ATR) spectroscopy are used to describe this technique in modern analytics [3-6].

The evolution of internal reflection accessories was driven by various optical geometries, applications, spectrometer development and availability of new materials. Fahrenfort used a variable angle system with a hemi-cylindrically shaped single reflection element made of KRS-5 [Tl(Br,Cl)] or silver chloride for the identification and quantification of samples as well as the determination of optical constants. Harrick discovered that using a multiple-reflection element increases the attenuation of the beam by the sample resulting in higher intensities of the bands in the spectrum [3-5].

Available spectrometers were dispersive and incorporated prism or grating monochromators. Therefore, the optical and mechanical geometry were restricted by the spectrometer's slits. They define the spectral resolution and limit the energy throughput as well as the geometry of the internal reflection element (IRE). Most of the spectrometers were designed as double beam instruments operating on the "optical-null" principle allowing for more accurate and faster collection of spectra [7, 8].

Early IRS attachments conformed to the vertical beam geometry of 20 mm height and could be configured to measure spectra of solids and liquids. Single-reflection IRE were triangular or hemi-cylindrically shaped, whereas multi-bounce ATR elements were available as a trapezoidal prism and parallelepiped. The former often uses variable-angle optics for the study of thin films or supported monolayers [9-11].

With the introduction of FTIR spectrometers, dispersive instruments were displaced. A beam of radiation is divided into two paths and then recombined after a certain path difference, thus leading to interferences. The resulting intensity of the beam emerging from the interferometer is measured as a function of the path difference yielding the interferogram. The spectrum is then calculated as the Fourier transform of the interferogram. The benefits of interferometers derive from the wavenumber precision (Connes) as well as the multiplex (Fellgett) and the throughput (Jacquinot) advantage allowing for faster measurements with higher signal-to-noise ratio than dispersive spectrometers [1, 12].

1.2. Concept of ATR-FTIR sensing

With the development of robust spectrometers, beam conduits, internal reflection flow cells and immersion probes, measurements in the process environment became feasible. The sample interface is typically separated from the spectrometer. Initially, flat trapezoidal or cylindrical multiple-reflection IREs were used, but probes with diamond sample-surface-contact are preferred as it offers high transparency for IR light and high chemical, mechanical and thermal stability. Several ATR-probes have been developed in the last few decades for in-line process and reaction monitoring as well as for in vivo studies [13-15].

ATR-FTIR spectroscopy is a great candidate for probing the characteristic vibrations of molecules in the fingerprint region of the spectrum [1, 6]. Cylindrical internal reflection elements are usually applied in measurements of liquids by enveloping them in a flow cell. At the ends of the rod parabolic mirrors are used to introduce light into the IRE and to reshape the exiting beam to conform to the expected beam path in the spectrometer [16].

In typical ATR-FTIR sensing schemes claddings are used to increase the selectivity and sensitivity by enriching the analyte in the probed volume of the evanescent field. Furthermore, these coatings can introduce additional benefits, for instance hydrophobicity to exclude water as seen in *Figure 1* to reduce background absorption, thus contributing to the increase in the cumulative depth of penetration. This concept has been proven on ATR crystals and optical fibres coated with polymers [17-19], mesoporous silica [20-22], zeolites [23, 24] or metal oxides [25] to detect volatile organic compounds in gas or aqueous phase.

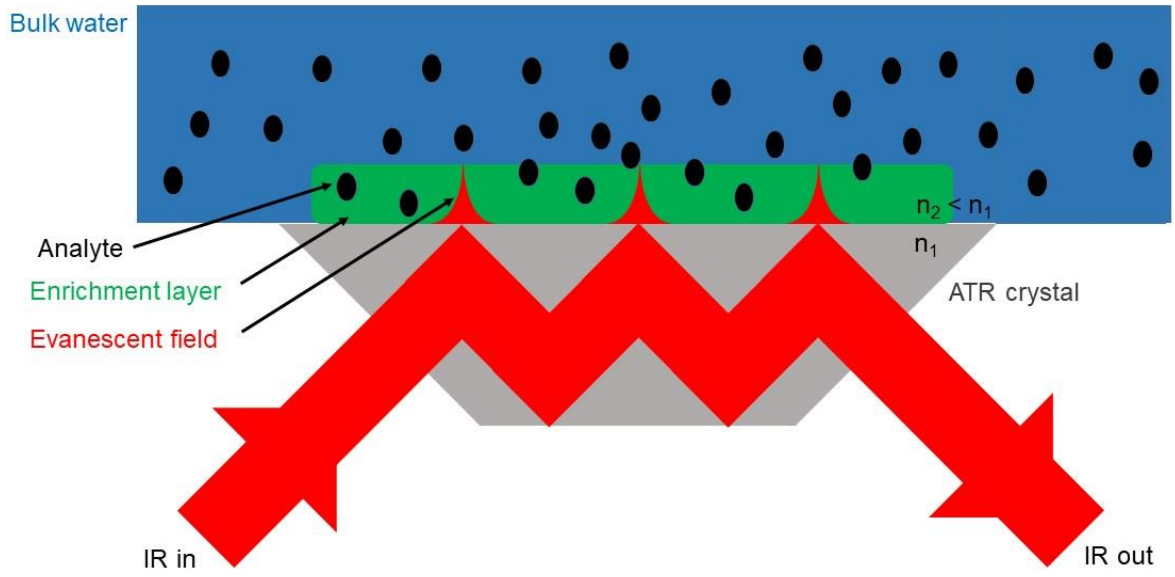

Figure 1: ATR-FTIR sensing scheme using enrichment layers.

1.3. Synthesis of mesoporous materials

Especially mesoporous materials show advantageous properties for sensing applications like high surface areas, adjustable porosity and pore size distribution as well as ample possibilities of chemical surface modifications [26-28]. Additionally, the rich surface chemistry of silica allows the introduction of functional groups, thus tuning the selectivity allowing for discriminating different analytes according to their size, polarity or functionality [29-31]. Due to their low refractive indices, they can be used as sensing layers in ATR spectroscopy as light will be reflected at the surface of the ATR element.

Mesoporous materials show both amorphous characteristics of gels and ordered porosity encountered in crystalline substances. The uniform, arranged pores have a tuneable pore size from 20 Å to 200 Å. These materials are typically synthesised by sol-gel processes using aggregates of surfactant molecules as structure-directing templates [32, 33].

Sol-gel chemistry describes the preparation of inorganic polymers or ceramics through a transformation of liquid precursors to a sol and finally to a network structure, which is often termed a gel. The sol is typically prepared by hydrolysis and condensation of metal alkoxide precursors [34]. The parameters influencing the formation of the sol like the water concentration or the pH-value as seen in *Figure 2* has been thoroughly studied. In acidic solutions, the rate of hydrolysis is higher than the rate of the condensation resulting in the formation of long chains, which eventually branch and cross-link during ageing. Under basic conditions, condensation is kinetically preferred and large agglomerates are formed, which cross-link during ageing [35].

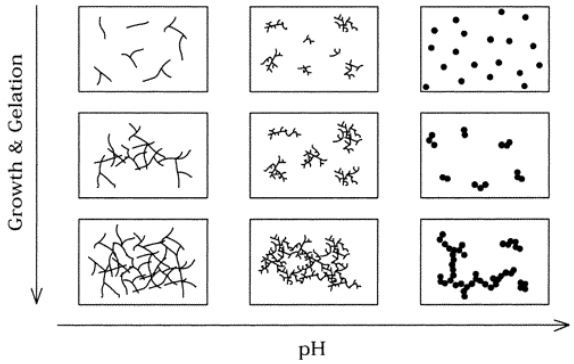

Figure 2: Effect of the pH-value on the particle-morphology in sol-gel reactions. Taken from ref. [35].

Mesoporous thin films are prepared by spin coating a pre-hydrolysed solution of a metal alkoxide precursor and a surfactant onto a substrate followed by drying at elevated temperatures to remove the solvent and to promote condensation of the precursors leading to the formation of a network. This process is known as evaporation induced self-assembly (EISA) [36]. No ordering is observed in the synthesis solution and the development of order requires a rapid evaporation of the solvent. Studies have shown the importance of water and solvent concentration in the atmosphere above the substrate during dip - or spin coating. Changing the relative humidity alters the content of water in the film resulting in phase changes from disordered to ordered mesostructures [37-39].

Characterisation of the mesostructure is typically performed by X-ray diffraction (XRD), grazing incidence-small angle X-ray scattering (GI-SAXS) and N_2 adsorption measurements for Brunauer-Emmett-Teller (BET) adsorption isotherms. From the diffraction peak positions, the pore structure can be determined. N_2 adsorption experiments are used to characterise the surface area, porosity and pore size distribution [40-43].

Additionally, the concentration of water in the sol, ageing time and the ratio of metal alkoxide to surfactant show a great influence on the mesophases formed during the coating process [38, 44, 45]. An example for the obtained mesophases from spin coating depending on the ratio of metal alkoxide to surfactant concentration and the ageing time of the sol at elevated temperatures is displayed in *Figure 3* [43].

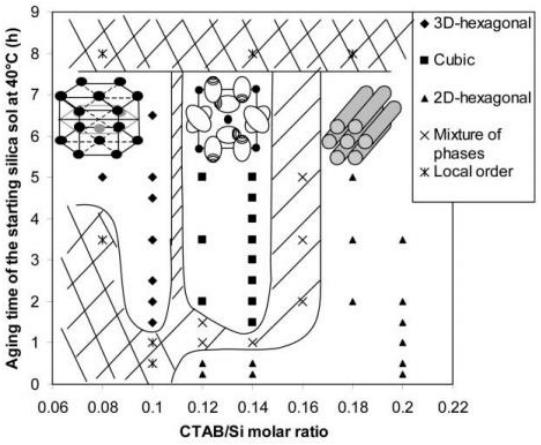

Figure 3: Resulting mesophases dependening on the ratio of metal alkoxide to surfactant and the ageing time of the sol at 40°C. Taken from ref. [43].

1.4. Aim of this work

Mesoporous silica has been widely applied in sensing schemes [20, 21, 29-31, 46], however, their application is limited by their poor chemical stability, especially in aqueous solutions at pH values above 8 [47, 48]. Furthermore, the strong absorption below 1200 cm^{-1} of the SiO_2 network prevents the analysis of various organic and inorganic sulphur- and phosphorus-containing compounds, for instance sulphates and phosphates [49].

For these reasons, the main objective of this work was the development of a mesoporous zirconia coating on ATR-crystals and testing its applicability in ATR-FTIR based sensing schemes.

First, an optimised preparation of a mesoporous ZrO_2-coating on Si- and Ge-ATR crystals had to be established. The chemical but also the thermal stability had to be ensured to be able to use this coating in different chemical environments.

Secondly, modification of the surface was necessary for applying this coating in sensing schemes involving more hydrophobic analytes and to keep water from penetrating the evanescent field of the IR beam.

Finally, the modified and pristine coating on ATR-crystals had to be applied in enrichment studies of various analytes and the process observed with FTIR spectroscopy. These experiments should determine the applicability of mesoporous ZrO_2-layers in evanescent wave based MIR sensing schemes.

2. Materials and methods

2.1. Methodology

FTIR spectra were collected using a Vertex 80v spectrometer (Bruker Optics, Ettlingen, Germany) operated with the OPUS 7.5 software. A mercury-cadmium-telluride (MCT) detector cooled with liquid nitrogen was used. All IR spectra were collected with a spectral resolution of 4 cm^{-1} and a total of 64 scans except for the IR spectra of enrichment studies, where 16 scans were averaged for each spectrum. Scans were obtained in double-sided, backward forward acquisition mode. The aperture was set to 6 mm to receive the best signal-to-noise ratio. Typically, 2000 to 4000 counts were obtained at the analogue-digital converter (ADC) for uncoated ATR crystals. For the enrichment studies, the computed absorbance spectra were converted to ascii-files in OPUS and evaluated using MATLAB R2020a. In that software the baseline subtraction as well as the integration of IR bands was carried out. For baseline subtraction, 5 data points on each side of the peak were averaged and the 2 average data points used to generate a linear function, which was subtracted from the peak. Then, using the *trapz* function of MATLAB R2020a, the peak areas were integrated. *Figure 4* illustrates the general idea. The curve representing the spectrum is displayed in blue, the data points used to generate a linear function in red and the obtained peak area in green.

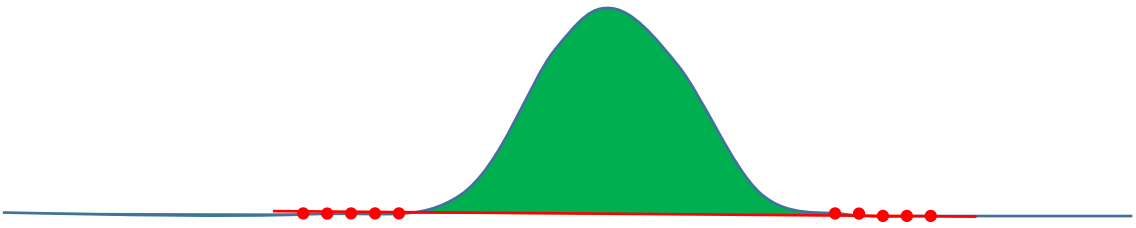

Figure 4: Illustration of the calculation of the peak areas.

The home-built ATR mount aka *Clipsi* and an aluminium flow cell with a volume of 20 µL designed by B. Baumgartner was used for the collection of ATR-FTIR spectra. Both are described in her Dissertation [50]. The ATR mount placed in the sample compartment of the Vertex 80v spectrometer without and with the aluminium flow cell is displayed in *Figure 5a* and *Figure 5b*, respectively. A stainless steel tubing (1/16'', 0.75 mm I.D.) inlet was attached to the flow cell as well as a PTFE tubing (1/16'', 0.75 mm I.D.) outlet. For the connection of the tubings, two low-dead volume SS-100-6-2AN fittings (Swagelok, USA) were used. Liquids were transported using a peristaltic pump from Ismatec (Grevenbroich, Germany).

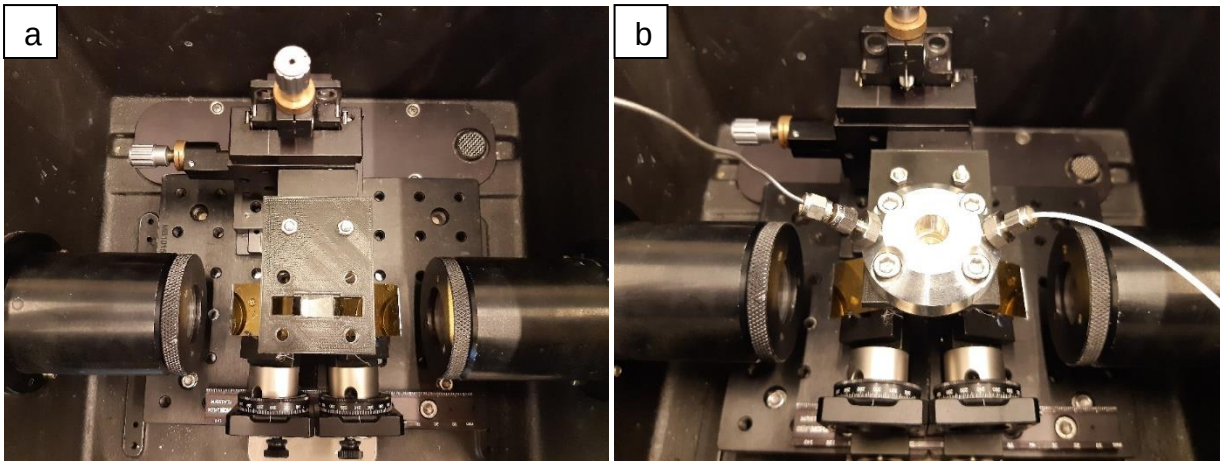

Figure 5: ATR mount aka Clipsi in the sample compartment of a Vertex 80v spectrometer (a) without flow cell and (b) with flow cell.

Double-side polished 10 mm x 20 mm x ~525 µm Si- and Ge-wafers were provided by the IMEC research group at Ghent University. The wafers were glued to an aluminium holder with a defined angle of 45° using wax. Then, the facets were polished using Al_2O_3 with a grain size of 30 µm and 9 µm followed by diamond with a grain size of 3 µm, 1 µm and 0.1 µm. They were polished in the sample preparation lab of USTEM at TU Wien. The obtained ATR-crystals were ultrasonically cleaned in acetone for 15 min.

Spin coating was performed using a SPIN150i-NPP spin coater by SPS-Europe GmbH (Ingolstadt, Germany). Prior to spin coating, the substrates were ultrasonically cleaned in ethanol for 15 min. The relative humidity in the chamber was controlled by mixing streams of dry and humidified air using two rotameters. Humidified air was obtained by bubbling dry air through a gas-washing bottle filled with water. The humidity was determined using a hygrometer (Testo GmbH, Wien, Austria) and the two streams were adjusted accordingly to obtain the desired relative humidity. 50µL of the precursor solution were deposited onto the substrate using a piston pipette.

Microscopic images and IR spectra in reflection mode were collected using a Hyperion 3000 FTIR microscope (Bruker Optics, Ettlingen, Germany) attached to a Tensor 37 (Bruker Optics, Ettlingen, Germany). The OPUS 7.8 software was used for controlling the microscope and spectra evaluation. The liquid nitrogen cooled MCT detector of the microscope was selected and spectra were recorded with a spectral resolution of 4 cm^{-1}, 128 scans, obtained in double-sided, backward forward acquisition mode. The aperture of the FTIR spectrometer was set to 6 mm.

UV/Vis spectra were collected using a Cary® 50 Bio UV-Vis spectrometer (Agilent Technologies, Santa Clara, California, USA) between 190 nm and 800 nm. Spectra were collected using the Cary WinUV software. A quartz cuvette with a path length of 10 mm was used for the analysis of liquids.

XRD patterns were collected using an X'Pert Pro diffractometer and the Data Collector software by PANalytical (Almelo, Netherlands). This instrument was equipped with a Cu anode, where a voltage of 45 kV and a current of 40 mA was applied resulting in a wavelength of 1.54 Å. A Bragg-Brentano geometry was used with 0.04 rad Soller slits and a divergence slit of ¼° as well as an anti-scatter slit of 1° in the incident beam path. An anti-scatter slit of 5.0 mm was used in the diffracted beam path and an X'Celerator detector. Samples were fixed onto a Si single crystal sample stage using Vaseline. XRD patterns were recorded at ambient temperature between 1° and 6° with a step size of 0.01° and a counting time of 60 s at each step. The sample holder was rotated with a rotation time of 4 s. Evaluation of the wide angle XRD patterns was performed using the HighScore Plus software by PANalytical (Almelo, Netherlands).

Non-ambient XRD measurements were conducted using an Empyrean multipurpose diffractometer and the Data Collector software by PANalytical (Almelo, Netherlands) equipped with an HTK-1200N chamber (Anton Paar, Graz, Austria). Samples were placed in the chamber on the ceramic sample holder and fixed with a thermal paste. The same configurations as mentioned for XRD patterns were used for the measurement.

GI-SAXS measurements were conducted using an Empyrean multipurpose diffractometer and the Data Collector software by PANalytical (Almelo, Netherlands) equipped with a Cu anode, where a voltage of 45 kV and a current of 40 mA was applied resulting in a wavelength of 1.54 Å. A focusing X-ray mirror, a divergence slit of $^{1}/_{32}$° and a GaliPIX3D detector were used. The measurement was conducted as described by the guideline of PANalytical. The collected diffraction patterns were evaluated using the XRD2DScan software by Panalytical (Almelo, Netherlands).

Raman spectra were collected using the Raman microscope LabRAM (Horiba Jobin Yvon GmbH, Bensheim, Germany) and the LabSpec6 sofware. The sample was mounted on the sample platform and focused using a 100x LWD objective. A laser with a wavelength of 532 nm and 45 mW was used for sample analysis. Prior to the measurements a calibration was performed using the vibration at 520.5 cm^{-1} of a pure Si-wafer.

Contact angle measurements were performed using a drop shape analyser (DSA) 30 by Krüss (Hamburg, Germany) in combination with the provided ADVANCE 1.5.1.0 software. The device was equipped with a CCD camera with a resolution of 780x582 and it could record 60 frames per second and a software controlled inclinable stage. Static contact angles were determined by placing a drop of 3 µL water on the sample's surface. Data analysis was performed by the Young-Laplace method of the instrument software.

The film thickness was determined using a DektakXT® profilometer with the Vision64 software by Bruker (Ettlingen, Germany). Scratches were inflicted to the coating using a pincer after spin coating. The obtained data was analysed using the Data Analyzer of the software.

2.2. Chemicals

All chemicals were used without further purification.

Acetone (*VWR*, HiPerSolv CHROMANORM® for HPLC, ≥ 99.8 %), ammonium citrate tribasic (*Sigma-Aldrich*, ≥ 97 %), benzene (C_6H_6, *Roth*, ROTIPURAN® ≥ 99.5 % p.a.), benzonitrile (C_6H_5CN, *Sigma-Aldrich*, 99 %), cetyltrimethylammonium bromide (CTAB, *Sigma-Aldrich*, 99 %), chloroform ($CHCl_3$, *VWR*, anhydrous ≥ 99.5 % stabilised with iso-amylene, AnalaR NORMAPUR® analytical reagent), chlorotrimethylsilane (*TCI*, ≥ 98.0 %), ethanol (EtOH, *Chem-Lab*, 100 % p.a.), hydrochloric acid (HCl, *VWR*, 37 %), mandelic acid (*Sigma-Aldrich*, 99 %), potassium dihydrogenphosphate (KH_2PO_4, *Merck*, ≥ 99.5 % p.a.), Pluronic® F-127 (F-127, *Sigma-Aldrich*, BioReagent), sodium hydroxide (NaOH, *PanReac AppliChem*, ≥ 98.0 % p.a.), tetraethoxysilane (TEOS, *Sigma-Aldrich*, 99.5 %), trichloro(phenyl)silane (*TCI*, ≥ 98.0 %), triethoxy(octyl)silane (*TCI*, ≥ 97.0 %), valeronitrile (C_4H_9CN, *Sigma-Aldrich*, 99 %), zirconium(IV) propoxide ($Zr(OPr)_4$, AcroSeal™, *ACROS Organics™*, 70 wt% in 1-propanol)

2.3. Synthesis of mesoporous SiO_2

The mesoporous SiO_2-coating was synthesised as previously reported [21, 51]. A sol was prepared by diluting 2.08 g TEOS with 2.2 mL of EtOH and adding 0.9 mL of a 0.056 M solution of HCl in H_2O. The mixture was stirred for 3 h at 40°C. 0.041 g CTAB was dissolved in 0.5 mL EtOH, 0.5 mL of the reaction solution added and stirred for 5 min. The solution was spin coated at 2000 rpm for 30 s at a relative humidity (RH) of 50 % onto a Si-substrate, which was ultrasonically cleaned in EtOH for 15 min prior to deposition. Afterwards, the coated substrate was pre-treated at 110°C overnight, cooled to ambient temperature followed by calcination at 400°C for 5 h with a heating ramp of 1°C min^{-1}

3. Development of a mesoporous ZrO_2-coating for ATR-FTIR spectroscopy

Several methods for preparing ZrO_2 by sol-gel processes are reported in literature [52-54]. Additionally, the preparation of mesoporous Zr-containing materials as well as ZrO_2-coatings have been developed [55-58]. However, none have reported a mesoporous ZrO_2-coating for sensing applications using ATR-FTIR spectroscopy.

For the synthesis of a mesoporous ZrO_2-coating, the following process was used: First, a precursor solution with a molar composition of 1.0 $Zr(PrO)_4$: 0.0075 F-127 : 2.4–3.6 HCl : 35.2 EtOH was prepared, which was then deposited on Si-wafers by spin coating at 3100 rpm for 20 s [56].

As no exact amount of HCl is given in literature, both the highest and lowest amount were tested for spin coating at 3100 rpm for 20 s. However, the prepared coatings showed visible inhomogeneity and were deemed unsuitable for further usage.

Studies report the importance of the chemical composition of the precursor solution as well as other parameters during spin coating, for instance the relative humidity (RH) [37-39]. Thus, the previously mentioned molar composition of the precursor solution was used, but spin coating and ageing parameters were adapted. First, the solution with the lowest amount of HCl was spin coated at different rotation speeds and for different time intervals until a homogenous coating was discernible. This was achieved at 2000 rpm for 30 s.

Then, the influence of the ageing process was investigated using spin coated Si-wafers as samples. The idea was to keep each sample at ambient temperature for 2 h and then at 60°C, 110°C, 150°C and 185°C for 2 d each after spin coating. Samples were removed from the oven at half time and at the end of every temperature step. After cooling to ambient temperature the obtained coatings of each sample were analysed by XRD.

The first ageing process and the corresponding XRD patterns are displayed in *Figure 6a* and *Figure 6b*, respectively.

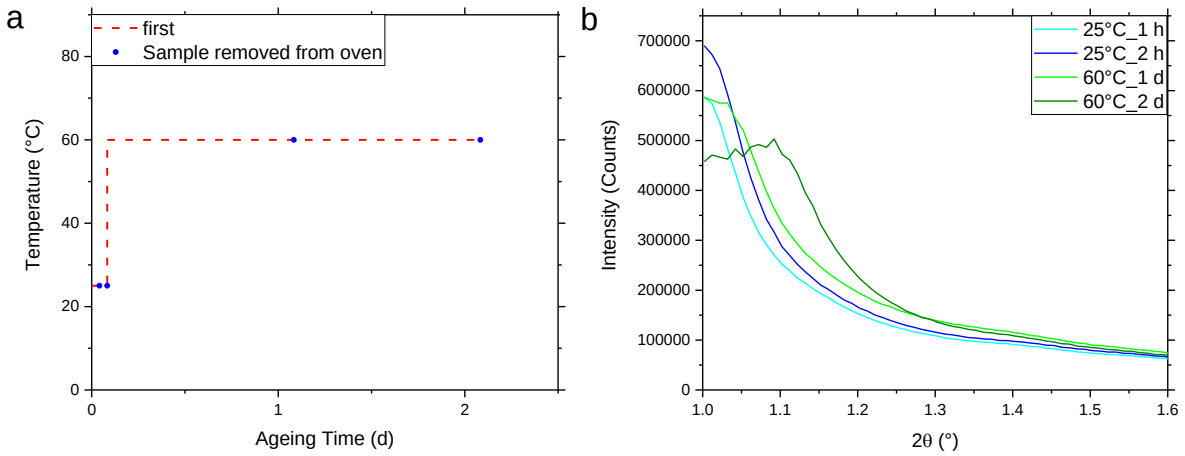

Figure 6: (a) First ageing process with markers representing samples, which were removed from the oven at the displayed ageing time and temperature and (b) the corresponding XRD patterns.

The red dashed line in *Figure 6a* shows the temperature program. The blue markers represent individual samples, which were removed from the oven at the displayed ageing time and temperature. The corresponding XRD patterns are displayed in *Figure 6b*. A decrease in diffraction peak intensity is visible when keeping the coating at 60°C for 2 d. Thus, for the next ageing process the ageing time of the temperature step at 60°C was decreased to 1 d to prevent the decrease in diffraction peak intensity.

The optimised ageing process is displayed in *Figure 7a* as well as the corresponding XRD patterns in *Figure 7b*.

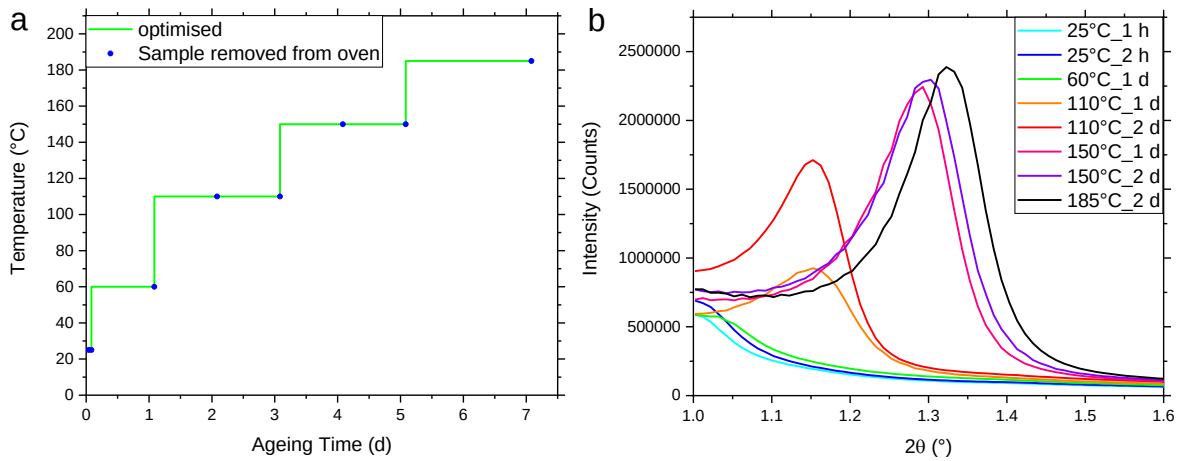

Figure 7: (a) Optimised ageing process with markers representing samples, which were removed from the oven at the displayed ageing time and temperature and (b) the corresponding XRD patterns.

The green solid line in *Figure 7a* shows the optimised temperature program and the blue markers represent individual samples, which were removed from the oven at the displayed ageing time and temperature. The corresponding XRD patterns are displayed in *Figure 7b*. As no decrease in diffraction peak intensity is observed for any sample, an optimal ageing process has been found. Upon increasing the temperature, a shift to higher diffraction angles (2θ) is visible. According to Bragg's law, this corresponds to a decrease in interplanar spacing (d-spacing), which is typically associated with contraction of the structure [59, 60].

The influence of the RH during spin coating of precursor solutions with the highest and lowest amount of HCl was determined. XRD patterns were collected after the ageing process and the intensity of the diffraction peak was used for the evaluation. From now on, precursor solutions with the lowest and highest amount of HCl will be referred to as L- and H-solution, respectively. The XRD patterns of the coatings of the L-solution spin coated at different RHs are displayed in *Figure 8*.

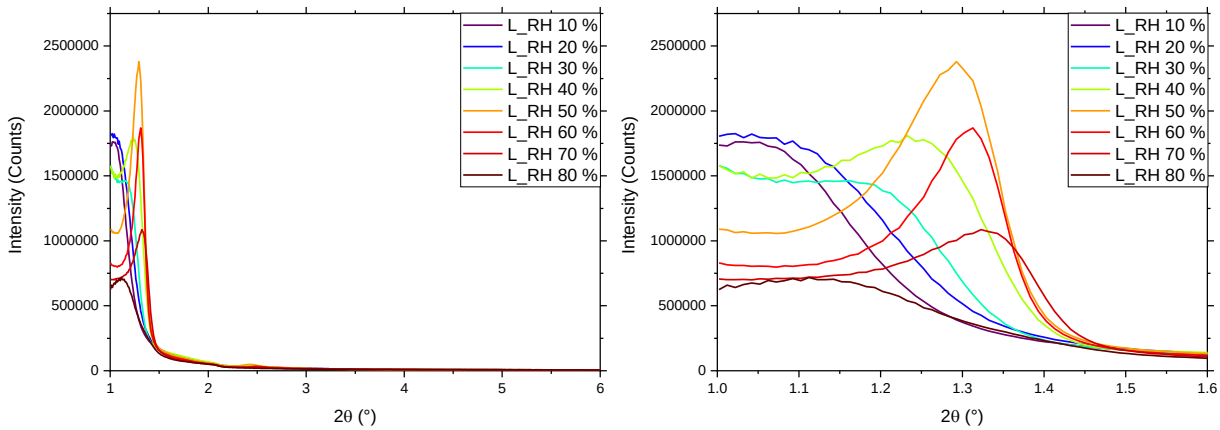

Figure 8: XRD patterns of the coatings of the L-solution spin coated at different RHs.

For the coatings of the L-solution, the highest intensity of the diffraction peak is obtained at a RH of 50 %. Lower RHs result in reduced intensities of the diffraction peak and shifts to lower 2θ. At higher RHs decreased intensities are observed as well, however, shifts to higher 2θ are seen except for the RH of 80 %, where a shift to lower 2θ is visible.

The XRD patterns of the coatings of the H-solution spin coated at different RHs are displayed in *Figure 9.*

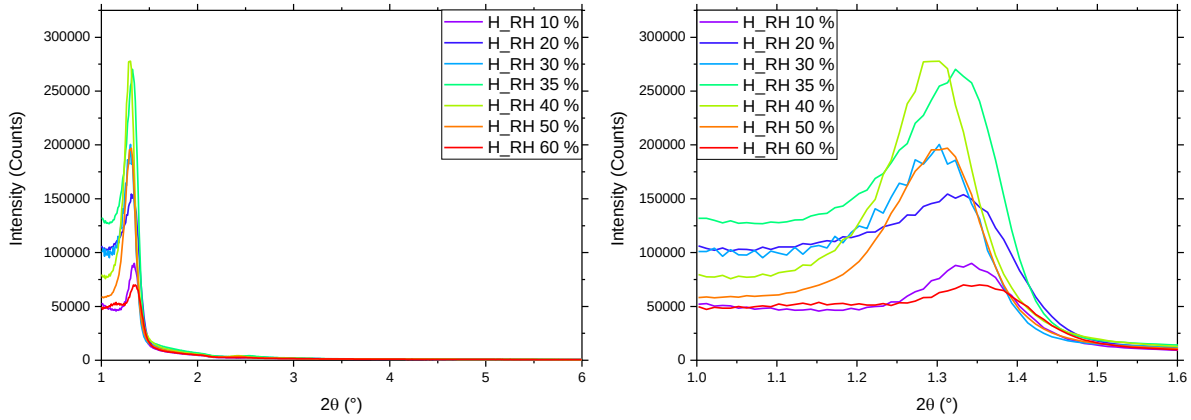

Figure 9: XRD patterns of the coatings of the H-solution spin coated at different RHs.

For the coatings of the H-solution, the highest intensity of the diffraction peaks is obtained at RHs of 35 % and 40 %. However, the former shows an increased area indicating a higher degree of ordering. Therefore, the optimal RH for this coating is 35 %. Shifts of the diffraction peak are less profound for these coatings compared to the shifts in *Figure 8*.

The optimal RHs during spin coating of precursor solutions were determined, which are 50 % and 35 % for spin coating the L- and H-solution, respectively. From now on, coatings from the L-solution spin coated at 50 % will be called L_RH 50 %-coating and coatings from the H-solution spin coated at 35 % will be called H_RH 35 %-coating.

The L- and H-solution were both spin coated onto Si-ATR crystals at a RH of 50 % and 35 %, respectively. After the ageing process, FTIR spectra were collected. The single channel spectra of an uncoated and the coated Si-ATR crystals are displayed in *Figure 10a*. The absorbance spectra of the coated Si-ATR crystals are seen in *Figure 10b*.

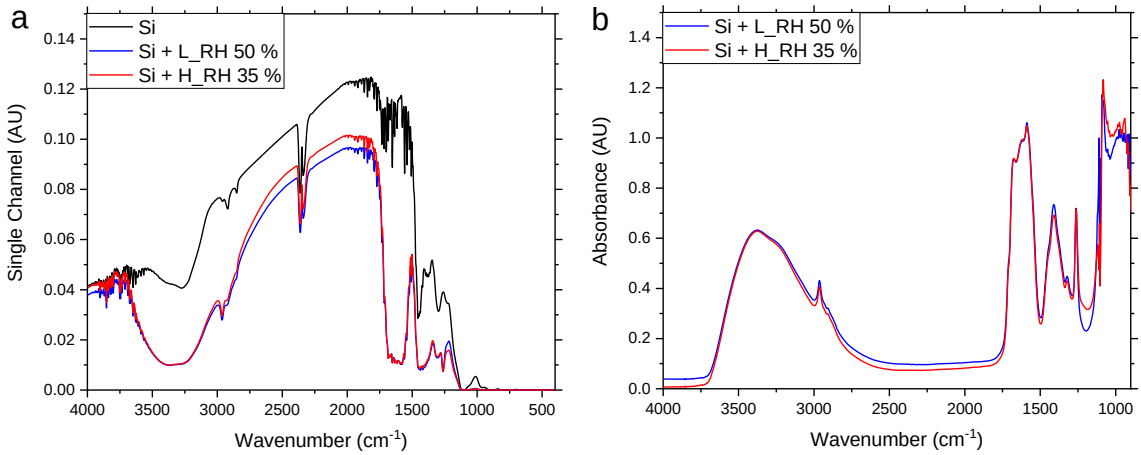

Figure 10: (a) FTIR single channel spectra of Si-ATR crystals without coating and with the L_RH 50 %- and H_RH 35 %-coating. (b) FTIR absorbance spectra of the Si-ATR crystals with the L_RH 50 %- and the H_RH 35 %-coating.

The absorbance spectra of the Si-ATR crystals with the coatings are now discussed in more detail. Thus, the areas of interest are enlarged and displayed in *Figure 11*.

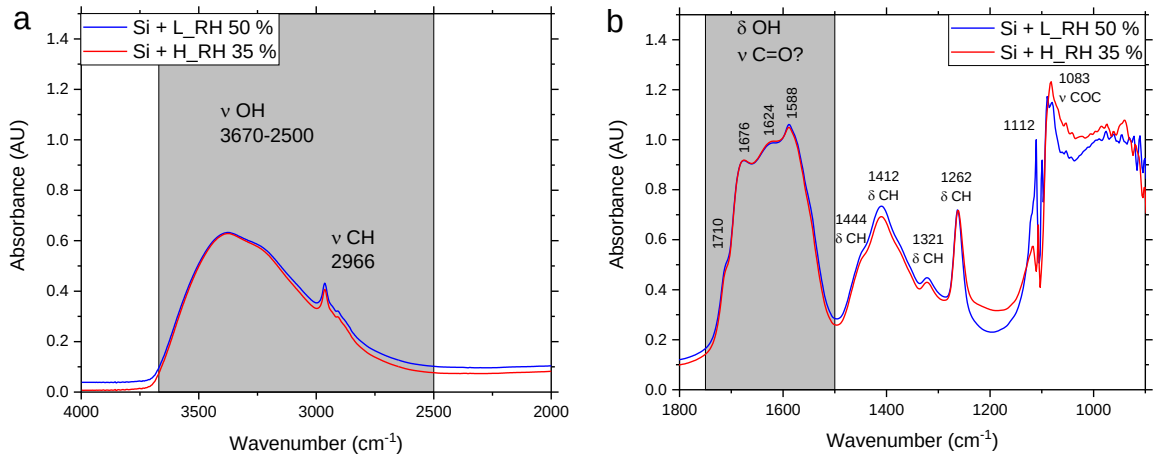

Figure 11: FTIR absorbance spectra of Si-ATR crystals with the L_RH 50 %- and the H_RH 35 %-coating from (a) 4000 cm^{-1} to 2000 cm^{-1} and (b) from 1800 cm^{-1} to 900 cm^{-1}.

Both coatings show a broad band between 3670 cm^{-1} and 2500 cm^{-1}, which is typically associated with the OH stretching vibration [49]. The band at 1112 cm^{-1} will later be discussed in more detail.

A band at 2966 cm^{-1} can be assigned to CH stretching vibrations. Bands between 1750 cm^{-1} and 1500 cm^{-1} correspond to C=O stretching vibration of carbonyl species [49]. The origin of these vibrations is peculiar as all substances used in the experiments do not contain carbonyl groups. However, the bands may be attributed to adsorbed CO_2. Studies have shown that the adsorption of CO_2 on monoclinic and tetragonal ZrO_2 produces bicarbonate, monodentate, bidentate and polydentate carbonates. Both monoclinic and tetragonal ZrO_2 show bands of HCO_3^- as well as bidentate carbonate in this region [61, 62]. The strong absorbance is probably caused by the large surface area of the mesoporous coating and, therefore, the high amount of adsorbed CO_2.

Several bands between 1500 cm^{-1} and 1200 cm^{-1} can be assigned to CH bending vibrations. The strong absorption band at 1083 cm^{-1} is a prominent feature in IR spectra of polyether corresponding to the COC stretching vibration. This band as well as the CH bands indicate that the surfactant Pluronic® F-127 is still present in the coatings. A spectrum of the surfactant is given in *Figure 12*.

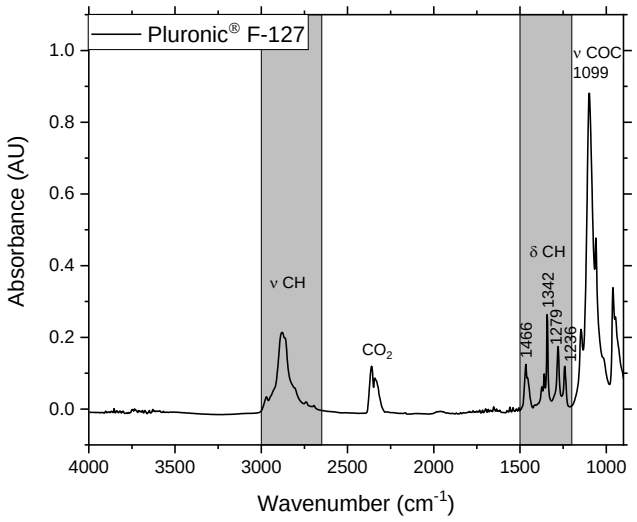

Figure 12: ATR-FTIR spectrum of solid Pluronic® F-127.

Therefore, tests to remove the surfactant were conducted. First attempts focussed on solvent extractions with EtOH and acetone, which damaged the coatings. Thus, calcination was chosen instead. To this purpose, temperature stability studies of the L_RH 50 %- and the H_RH 35 %-coating were conducted. Coated wafers were heated to 900°C and every 5°C a XRD measurement was collected. The resulting diffraction patterns for the L_RH 50 %-coating are displayed in *Figure 13*.

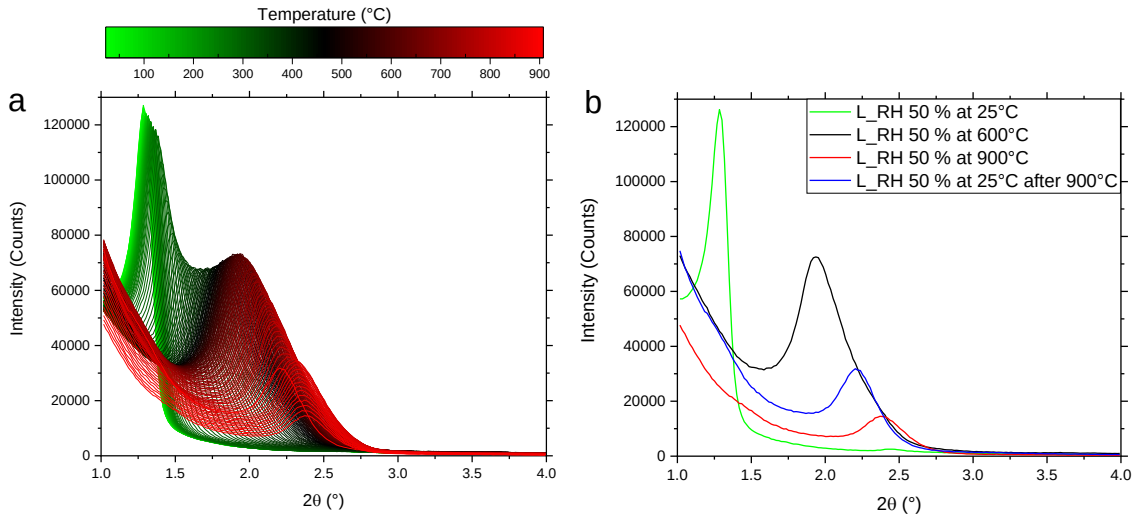

Figure 13: XRD patterns of the L_RH 50 %-coating at different temperatures. (a) For all temperature steps and (b) at 25°C, 600°C, 900°C and at 25°C after 900°C.

Upon increasing the temperature, the diffraction peak shifts to higher 2θ corresponding to a decrease in d-spacing according to Bragg's law. This is typically associated with contraction of the structure [59, 60]. The reduction in intensity is either caused by broadening of the diffraction peak or a decrease in mesoporous ordering. At 600°C a local maximum in intensity is reached with a 2θ value of 1.94°. At 900°C only a small diffraction peak is visible, whose intensity increases upon cooling the sample to 25°C, and the 2θ decreases corresponding to expansion. The diffraction patterns at the relevant temperature steps are displayed in *Figure 13b*.

The same procedure was performed with the H_RH 35 %-coating. The respective diffraction patterns are displayed in *Figure 14*.

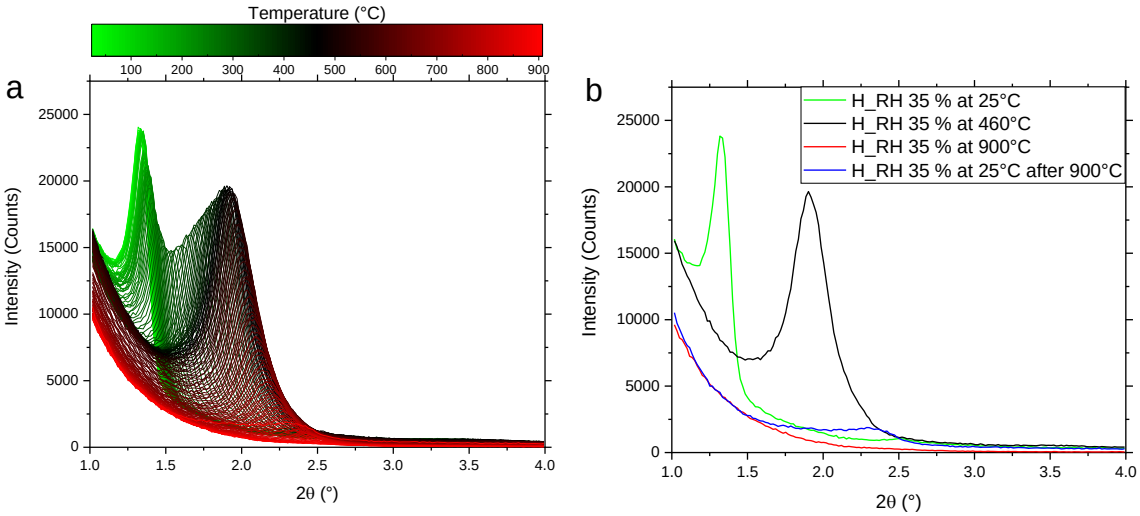

Figure 14: XRD patterns of the H_RH 35 %-coating at different temperatures. (a) For all temperature steps and (b) at 25°C, 460°C, 900°C and at 25°C after 900°C.

In *Figure 14a* the XRD patterns of the H_RH 35 %-coating at different temperatures are displayed. A similar trend compared to the L_RH 50 %-coating is obtained. However, the local maximum is reached at 460°C with a 2θ value of 1.90°. Additionally, at 900°C the diffraction peak is completely gone and after cooling to 25°C the intensity is only slightly increased. The diffraction patterns at the relevant temperature steps are displayed in *Figure 14b*.

This indicates a greater loss of the mesostructure for the H_RH 35 %-coating upon heating to 900°C compared to the L_RH 50 %-coating. The temperature-dependent intensity of the diffraction peak for the L_RH 50 %- and the H_RH 35 %-coating are displayed in *Figure 15a* and *Figure 15b*, respectively.

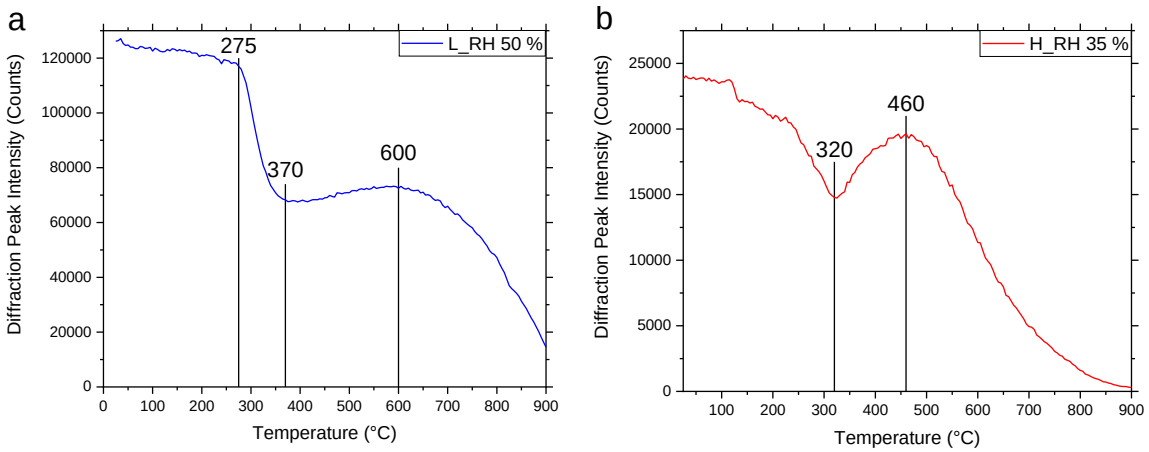

Figure 15: Temperature-dependent intensity of the diffraction peak for the (a) L_RH 50 %- and the (b) H_RH 35 %-coating.

The L_RH 50 %-coating shows a linear decrease in diffraction peak intensity at first with a change in slope at 275°C. At 370°C a local minimum is reached and the intensity gradually increases until a decrease at 600°C is seen. For the H_RH 35 %-coating the slope decreases continually until a local minimum at 320°C is reached. Then, the intensity shows a local maximum at 460°C followed by a decrease.

To investigate if the decrease in diffraction peak intensity is caused by recrystallisation processes, XRD patterns at higher 2θ were collected for both coatings. The results as well as the determined phases of an uncoated Si-wafer and the L_RH 50 %-coating before and after heating to 900°C are displayed in *Figure 16*.

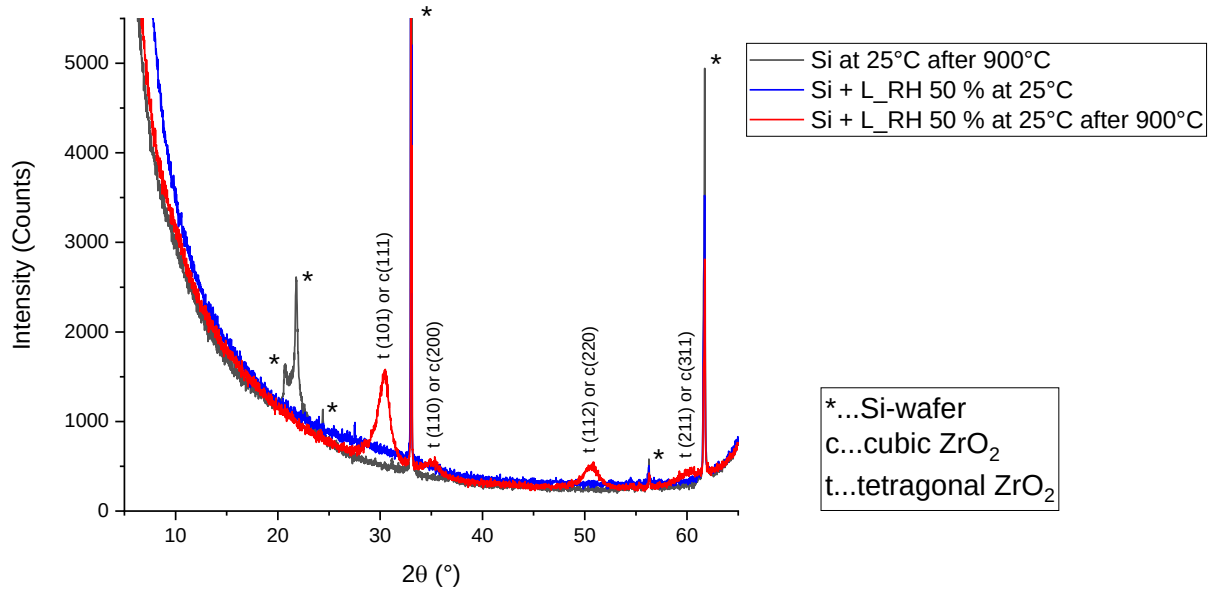

Figure 16: Wide-angle XRD patterns of the L_RH 50 %-coating before and after heating to 900°C and an uncoated Si-wafer after heating to 900°C.

Prior to the heat treatment, no XRD pattern at higher diffraction angles are found for the L_RH 50 %-coating. Afterwards, broad diffraction peaks attributed to a tetragonal or a cubic phase are present [63-66]. Interestingly, the Si-wafer without ZrO_2-coating shows additional diffraction peaks, which are not visible for the coated sample. Upon heating to 900°C recrystallisation occurred, which explains the decrease in the diffraction peak intensity at higher temperatures as seen in *Figure 13* and *Figure 15a*.

The XRD patterns as well as the determined phases of an uncoated Si-wafer and the H_RH 35 %-coating before and after heating to 900°C are displayed in *Figure 17*.

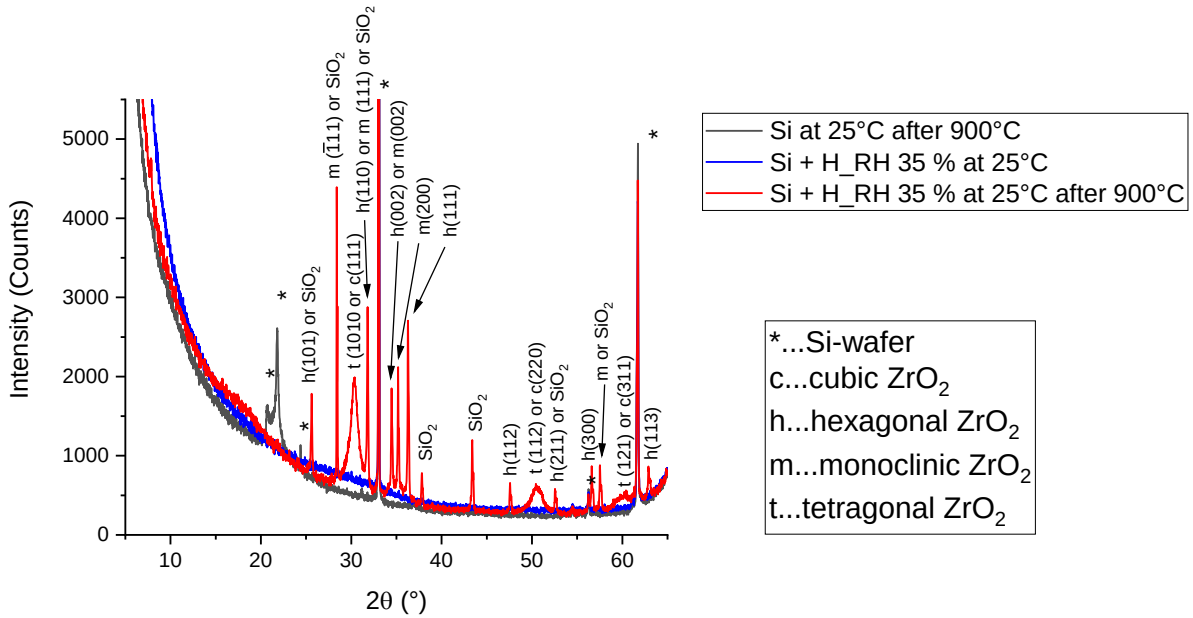

Figure 17: Wide-angle XRD patterns of the H_RH 35 %-coating before and after heating to 900°C and an uncoated Si-wafer after heating to 900°C.

The H_RH 35 %-coating shows no diffraction peaks prior to the heat treatment. However, after increasing the temperature to 900°C, several sharp and a few broad peaks are obtained. Similar to the L_RH 50 %-coating, diffraction peaks attributed to a cubic or tetragonal ZrO_2 phase are visible. Additionally, a hexagonal and a monoclinic phase as well as diffraction peaks from SiO_2 are found in the diffraction pattern [64, 65, 67-70]. Therefore, the H_RH 35 %-coating experiences recrystallisation to a higher degree resulting in a decreased diffraction peak intensity compared to the L_RH 50 %-coating.

To check if the difference in thermal stability of the coatings correlates with a deviation in film thickness, the latter was determined for both coatings after the ageing process. Additionally, three different Si-wafers with a L_RH 50 %-coating were measured to investigate the deviation of film thickness between single spin coating processes.

To obtain the spatial distribution of the film thickness, the following three measurement areas on each sample were chosen: One in the centre, where the solution was applied during spin coating, and two near the opposite edges of the wafer as displayed in *Figure 18a*. The grey lines represent scratches on the ZrO_2-coating, which were inflicted directly after spin coating. For each area, R1, C and R2, three measurements were performed at the positions indicated by the red vertical lines.

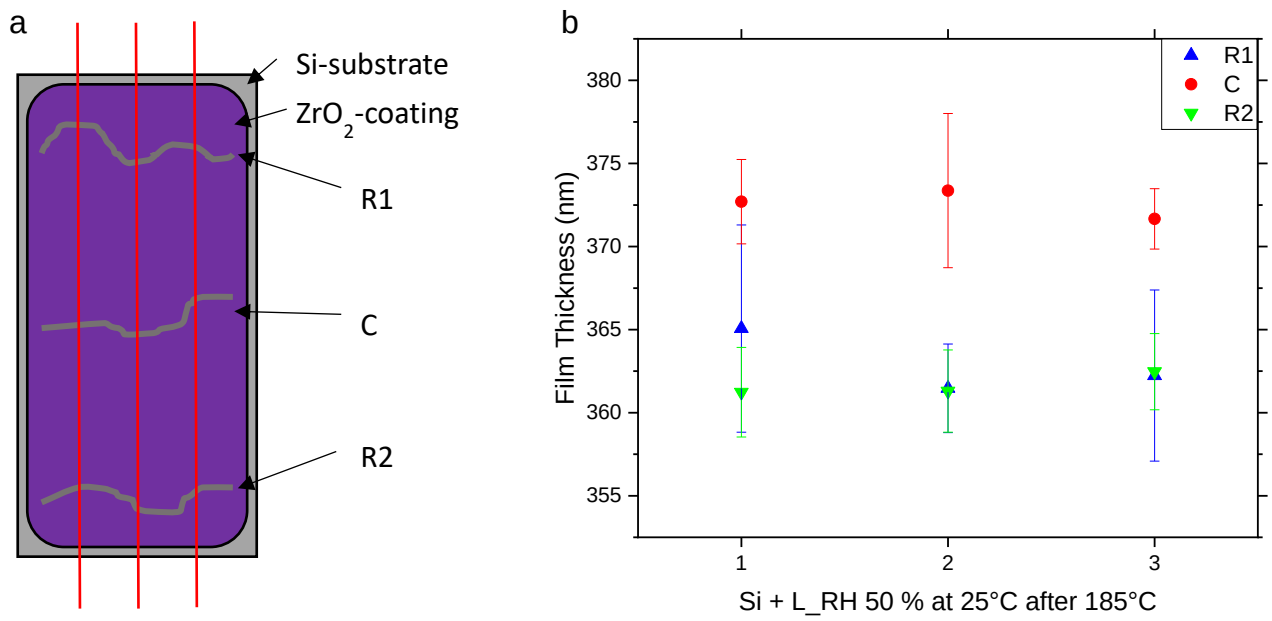

Figure 18: (a) Schematic of the measurement areas for each sample and (b) the resulting film thickness of the measurement areas for three individual Si-wafers with the L_RH 50 %-coating.

As seen in *Figure 18b* all three samples show a similar spatial distribution of the film thickness, but higher values are obtained for measurement area C. This is expected, as the precursor solution is applied in the centre of the wafer during spin coating, which is then transported to the edges by the centrifugal force. However, the relative difference in film thickness between C and the areas R1 and R2, respectively, are between 2 % and 3 %. Therefore, the spatial distribution is neglected for further evaluations and an average film thickness of the whole coating is used instead.

The average film thickness of the L_RH 50 %- and the H_RH 35 %-coating after the ageing process is displayed in *Figure 19*.

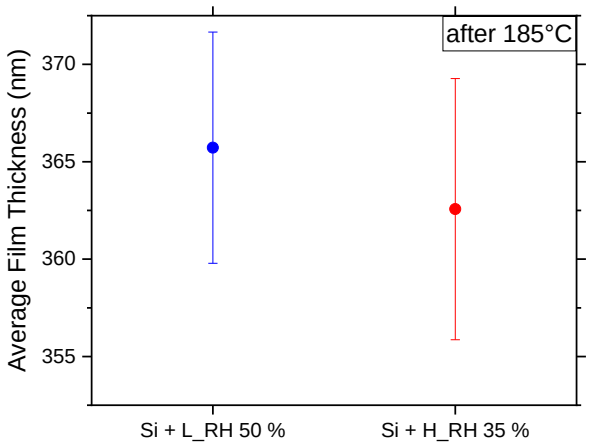

Figure 19: Comparison of the average film thickness of the L_RH 50 %- and the H_RH 35 %-coating.

The H_RH 35 %-coating only shows a slightly lower film thickness compared to the L_RH 50 %-coating, but considering the errors displayed in *Figure 19* the film thicknesses are equal. So it can be concluded, that the poorer thermal stability of the H_RH 35 %-coating is not caused by a deviation in film thickness, but possibly by a lower degree of condensation or a different chemical composition.

For the removal of the surfactant, a calcination process with a heating ramp of 1°C min^{-1} and a plateau at 500°C was chosen. The presence of the mesostructure was confirmed using XRD analysis. The XRD patterns before and after calcination at 500°C of the L_RH 50 %- and the H_RH 35 %-coating are displayed in *Figure 20*.

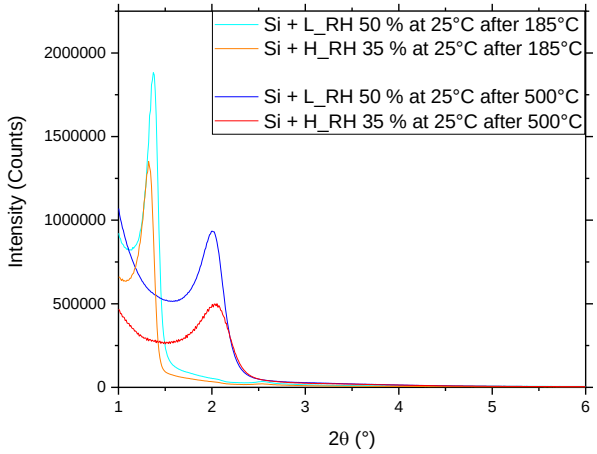

Figure 20: XRD patterns before and after calcination at 500°C of the L_RH 50 %- and the H_RH 35 %-coating.

As previously mentioned, the shift of the diffraction peak to higher 2θ corresponds to contraction processes during the heat treatment. Using Bragg's law, the d-spacing before and after calcination can be derived from the 2θ values and the wavelength of X-rays used for the analysis. Then, the contraction can be calculated as the difference in d-spacings before and after calcination divided by the d-spacing before calcination [59, 60].

The diffraction angles, the calculated d-spacings and contraction values are summarised in *Table 2*.

Table 2: Diffraction angles, calculated d-spacings before and after calcination at 500°C and contractions of the L_RH 50 %- and H_RH 35 %-coating.

Sample	2θ at 25°C (°)		d-spacing at 25°C (Å)		Contraction (%)
	after 185°C	after 500°C	after 185°C	after 500°C	
Si + L_RH 50 %	1.373	2.005	64.27	44.01	32
Si + H_RH 35 %	1.323	2.055	66.69	42.94	36

Additionally, the average film thickness after calcination of both the L_RH 50 %- and the H_RH 35 %-coating was measured. The results are compared to the average film thickness prior to calcination in *Figure 21*.

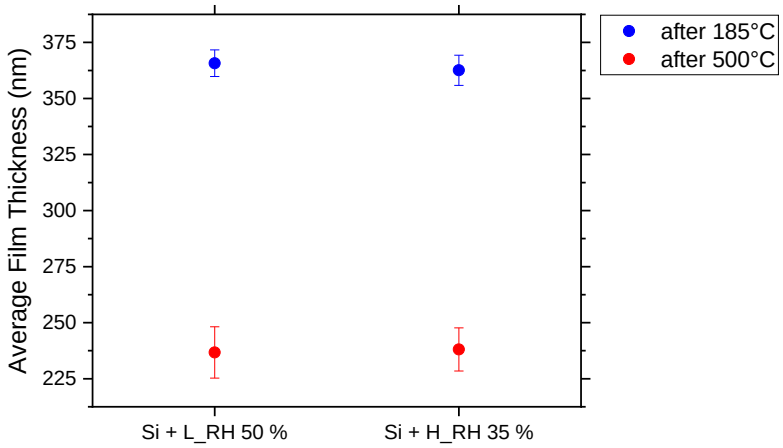

Figure 21: Average film thickness before and after calcination at 500°C for the L_RH 50 %- and the H_RH 35 %-coating.

The contraction of the film thickness was then calculated as previously done for the d-spacings. A summary of the average film thickness before and after calcination as well as the calculated contraction of both coatings is given in *Table 3*.

Table 3: Average film thickness before and after calcination at 500°C and the calculated contraction of the L_RH 50 %- and the H_RH 35 %-coating

Sample	Average film thickness at 25°C (nm)		Contraction (%)
	after 185°C	after 500°C	
Si + L_RH 50 %	365.7	236.7	35
Si + H_RH 35 %	362.6	238.0	34

The contraction of the L_RH 50 %- and the H_RH 35 %-coating calculated from the d-spacings are 32 % and 36 %, respectively. The obtained contraction calculated from the average film thickness are 35 % for the L_RH 50 %- and 34 % for the H_RH 35%-coating. Similar contractions are obtained independent of the parameters used for calculation. Additionally, the difference in contraction between both coatings is very small.

From this point forward only the L_RH 50 %-coating was further investigated as it shows a higher diffraction peak intensity, which indicates a more ordered mesostructure, and a higher thermal stability compared to the H_RH 35 %-coating.

After calcination at 500°C the L_RH 50 %-coating was analysed using FTIR spectroscopy to check for the presence of the surfactant. The spectra before and after calcination are displayed in *Figure 22*.

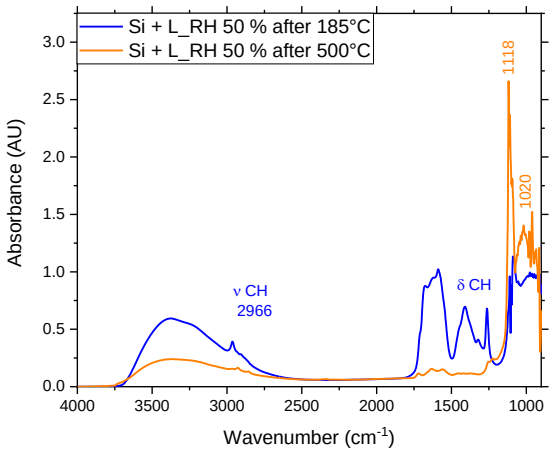

Figure 22: FTIR absorbance spectra of the L_RH 50 %-coating before and after calcination at 500°C.

The bands assigned to CH vibrations of the surfactant were no longer present after the calcination at 500°C. Therefore, it may be concluded that the surfactant Pluronic® F-127 was successfully removed from the coating. For simplicity, the L_RH 50 %-coating will be called the ZrO_2-coating from now on.

The bands at 1118 cm^{-1} and 1020 cm^{-1} increase in intensity after calcination. Literature suggests, that the former may be attributed to surface ZrOH bending vibrations [71]. However, the reference they cited never mentions any zirconia compounds [72], only another reference, which refers to a handbook of inorganic and coordination compounds. This book neither shows entries of zirconia compounds nor bending vibrations of coordinated ligands [73]. In addition, the band intensity increases after calcination, but the contraction seen in XRD patterns and in the average film thickness as well as the decrease in the broad band above 2500 cm^{-1} attributed to OH stretching vibrations suggests that condensation has taken place. Therefore, the intensity of free surface ZrOH should have been decreased.

This band may also be caused by SiO stretching vibrations [49], which were formed by the calcination of the Si-ATR crystal. A FTIR spectrum of a Si-ATR crystal with a mesoporous SiO_2-coating is displayed in *Figure 23a*. The coating shows a broad band below 1250 cm^{-1} attributed to the SiO_2 network. However, no SiO stretching vibrations appears in the single channel spectra of a Si-ATR crystal after calcination at 500°C as seen in *Figure 23b*. Therefore, the band at 1118 cm^{-1} cannot be attributed to SiO stretching vibrations.

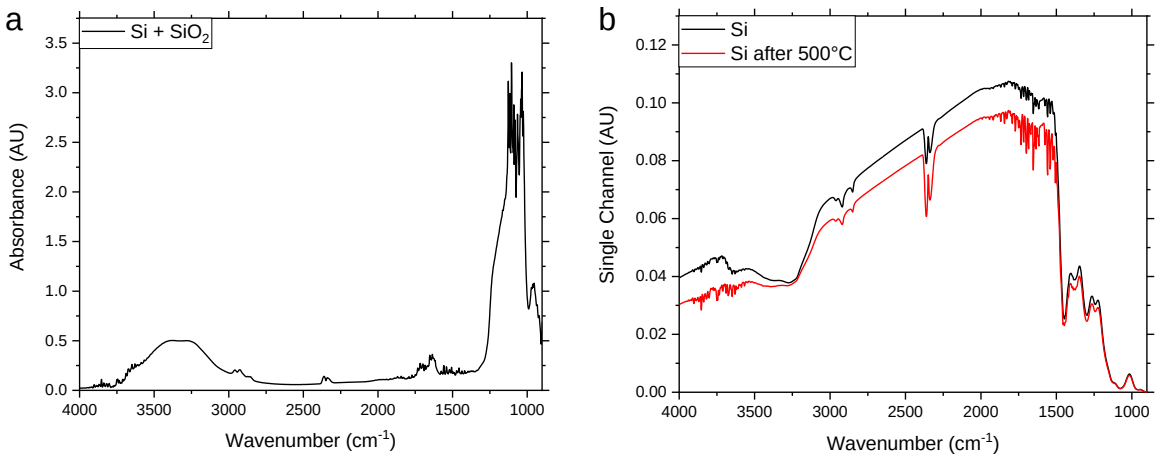

Figure 23: (a) FTIR absorbance spectrum of a Si-ATR crystal coated with mesoporous SiO_2. (b) FTIR single channel spectra of a Si-ATR crystal before and after calcination at 500°C.

As this band increases in intensity after calcination, it may be attributed to ZrO stretching vibrations or mixed ZrOSi stretching vibrations. Compared to the SiO system, Zr shows a higher mass, which would result in a shift to lower frequencies. Therefore, ZrO would need a higher bond strength to be located in the same wavenumber region as SiO. However, literature reports similar bond strengths for SiO and ZrO [74]. Additionally, literature reports the ZrO stretching vibration as well as the ZrOH bending vibrations below 800 cm^{-1}. However, every reference cited refers to another reference and so on. Thus, it cannot be confirmed that these vibrations are actually found below 800 cm^{-1}.

In conclusion, the assignment of the bands at 1118 cm^{-1} and 1020 cm^{-1} to a certain vibration was not possible and further research is needed to investigate the occurrence of these vibrations.

ZrO_2-coatings after the temperature treatments at 110°C, 150°C, 185°C and after calcination at 500°C were investigated using GI-SAXS measurements to obtain information about the mesostructure. The measured GI-SAXS patterns are displayed as heat maps in *Figure 24*. The blue and red colour correspond to a low and high intensity, respectively.

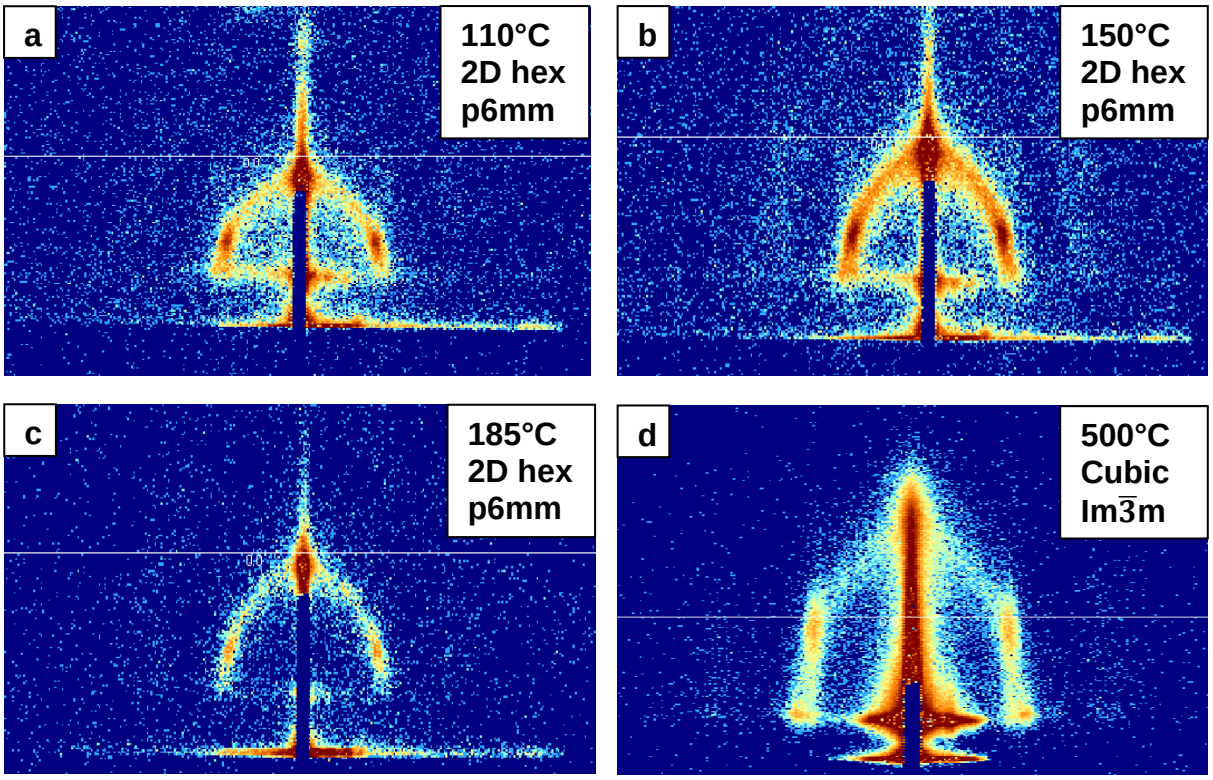

Figure 24: GI-SAXS patterns of the ZrO_2-coating and the assigned mesostructures after (a) 110°C, (b) 150°C, (c) 185°C and (d) after calcination at 500°C.

From the GI-SAXS patterns, a change in the mesostructure is visible. Up to 185°C, a diffraction pattern of a 2D hexagonal structure is obtained, but upon increasing the temperature to 500°C, a pattern associated with a cubic mesostructure appears [27, 75]. Phase transformations in the mesostructure from hexagonal to cubic have been extensively studied as well as the inverse process, which is usually caused by thermal treatment [76-78]. The formation of the cubic phase induces a higher degree of ordering resulting in an increase in the diffraction peak intensity associated with the mesostructure. This explains the temperature-dependent diffraction patterns displayed in *Figure 13* and *Figure 15a*.

Additionally, the thermal stability at 500°C for prolonged periods of time was investigated. Si-wafers with ZrO_2-coatings were heated to 500°C with a ramp of 1°C min^{-1}, calcined for different time intervals and cooled to ambient temperature. After this treatment XRD patterns were collected. The results of the small- and wide-angle XRD measurements are displayed in *Figure 25* and *Figure 26*, respectively.

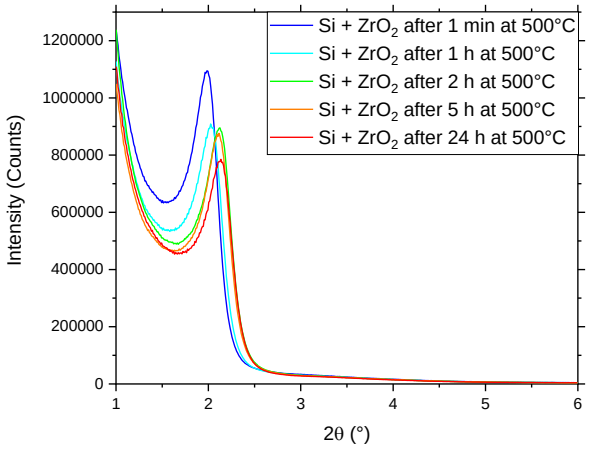

Figure 25: XRD patterns of the ZrO_2-coating after calcination at 500°C for 1 min, 1 h, 2 h, 5 h and 24 h.

The diffraction peak attributed to the mesostructure decreases with increasing calcination time at 500°C. The difference between 1 min and 1 h is profound, however, almost no distinction between 1 h, 2 h and 5 h at 500°C is discernible. Keeping the sample at 500°C for 24 h further decreases the diffraction peak intensity. Additionally, the peak shifts to higher 2θ with increasing the calcination time.

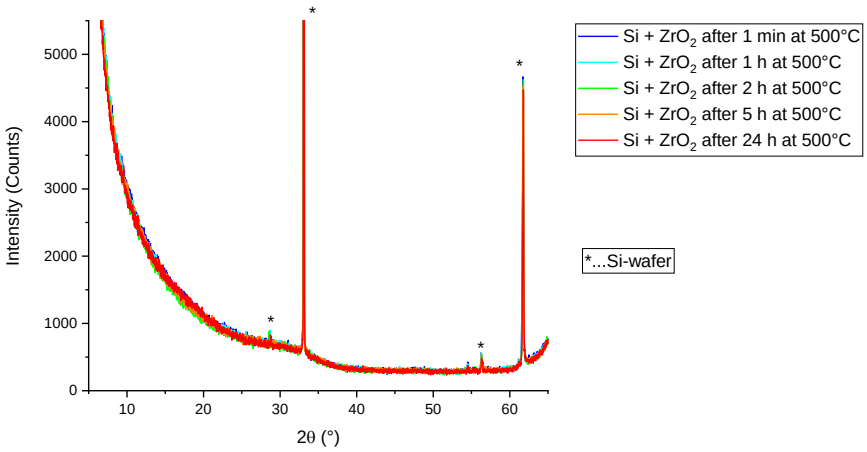

Figure 26: Wide-angle XRD patterns of the ZrO_2-coating after calcination for 1 min, 1 h, 2 h, 5 h and 24 h.

The wide-angle XRD patterns of all samples show identical diffraction patterns. The visible diffraction peaks are attributed to Si and SiO_2 [64, 65, 68], which are already present on the Si-wafer at ambient temperature as seen in the wide-angle XRD pattern of an uncoated Si-wafer displayed in *Figure 27*.

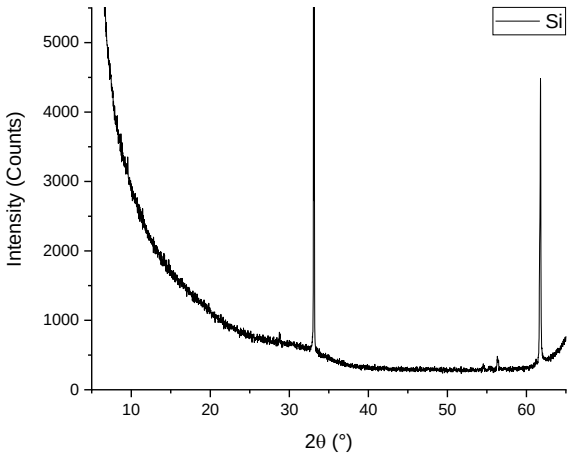

Figure 27: Wide-angle XRD pattern of an uncoated Si-wafer.

Thus, the thermal stability of the mesoporous ZrO_2-coating was confirmed. As no recrystallisation occurred at 500°C, the diffraction peak assigned to the mesostructure was still visible after several hours at 500°C. Only increasing the temperature well above 600°C induces recrystallisation processes and, consequently, destroys the mesostructure as previously seen.

Raman spectra of the coated Si-wafer were collected at various laser powers. However, distinction between the Si-substrate and the ZrO_2-coating is not possible. The same conclusion has to been drawn for ZrO_2-coated Ge-wafers. The Raman spectra of the ZrO_2-coating on Si- and Ge-wafers are provided in the Appendix.

For this reason, Au-sputtered CaF_2-substrates were coated with mesoporous ZrO_2 and analysed by Raman spectroscopy. The collected spectrum is displayed in *Figure 28*.

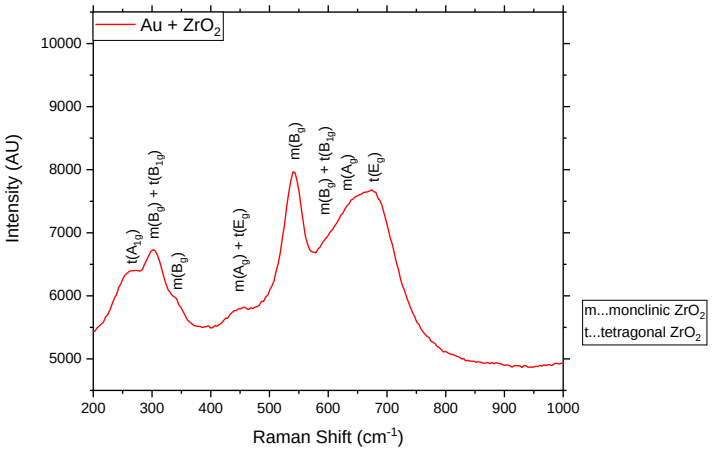

Figure 28: Raman spectrum of a ZrO_2-coated Au-sputtered CaF_2-substrate.

The Raman spectrum shows bands at 262, 302, 342, 449, 541 cm^{-1} and several overlapping bands between 590 cm^{-1} and 750 cm^{-1}. According to literature, these vibrations are associated with tetragonal and monoclinic ZrO_2 [70, 79, 80]. Even though no recrystallisation is seen in the XRD patterns, the symmetry of tetragonal and monoclinic ZrO_2 must be present in the coating.

Additionally, Ge-wafers and Ge-ATR crystals were coated with mesoporous ZrO_2, thermally treated as described in the optimised ageing process and calcined at 500°C using a ramp of 1°C min^{-1}. The presence of the mesostructure was confirmed by an XRD measurement of a Ge-wafer and the coating on a Ge-ATR crystal was analysed by FTIR spectroscopy as seen in *Figure 29a* and *Figure 29b*, respectively.

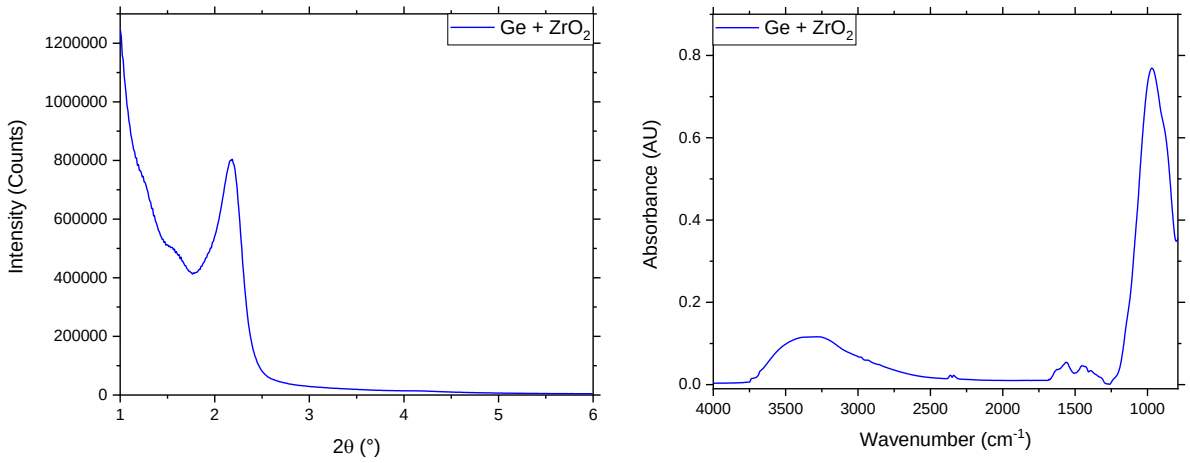

Figure 29: (a) XRD pattern of a ZrO_2-coated Ge-wafer and (b) FTIR absorbance spectrum of a ZrO_2-coated Ge-ATR crystal.

The strong absorption band around 1000 cm^{-1} cannot be explained as previously discussed. Compared to the coated Si-substrates in *Figure 22*, this vibration appears at lower wavenumbers indicating a weaker strength in chemical bonding or a higher mass. The chemical bond strength found in literature is lower for GeO than for SiO and the former shows a higher mass [74]. Therefore, the stretching vibration of GeO would be expected at even lower wavenumbers as seen in transmission spectra of GeO_2 in literature [81]. As this band only appears after applying the ZrO_2-coating and at lower wavenumbers compared to the coated Si-substrates, the interface of the Ge-substrate and the coating may be causing this band. Therefore, it may be attributed to a ZrOGe stretching vibration, however, further research is necessary to assign this band.

Additionally, the average film thickness of the ZrO_2-coating on the Ge-substrate after calcination at 500°C was measured and compared to the ZrO_2-coating on the Si-substrate as seen in *Figure 30*.

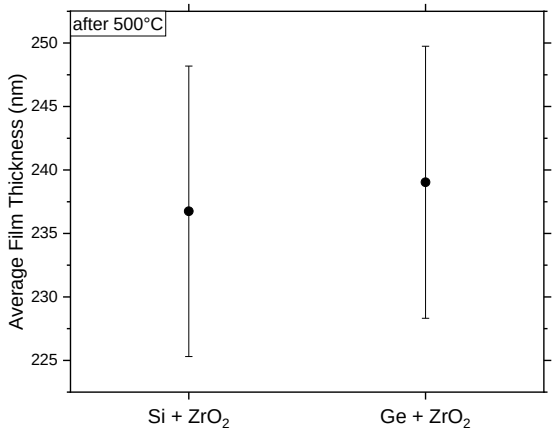

Figure 30: Average film thickness of the ZrO_2-coating on the Si- and Ge-substrate.

The ZrO_2-coatings on both Si and Ge show a similar average film thickness and considering the errors displayed in *Figure 30* no difference between Si- and Ge-wafers for the average film thickness is discernible.

The chemical stability of the ZrO_2-coating was investigated and compared to a prepared SiO_2-coating. The latter was synthesised as described in section 2.3. According to literature, SiO_2 should be stable at pH-values below 7 and ZrO_2 chemically inert at pH-values from 1 through 14 [47, 82]. As both SiO_2 and ZrO_2 should be stable in acidic solution, a higher pH-value was investigated. Thus, both coatings were placed in a flask, which was then filled with an aqueous 0.01 M NaOH solution. A pH-value of 12 was measured for this solution.

Microscopic images were taken and IR spectra in reflexion mode were collected using a FTIR microscope. Images before and after treatment with the aqueous NaOH solution are displayed in *Figure 31*.

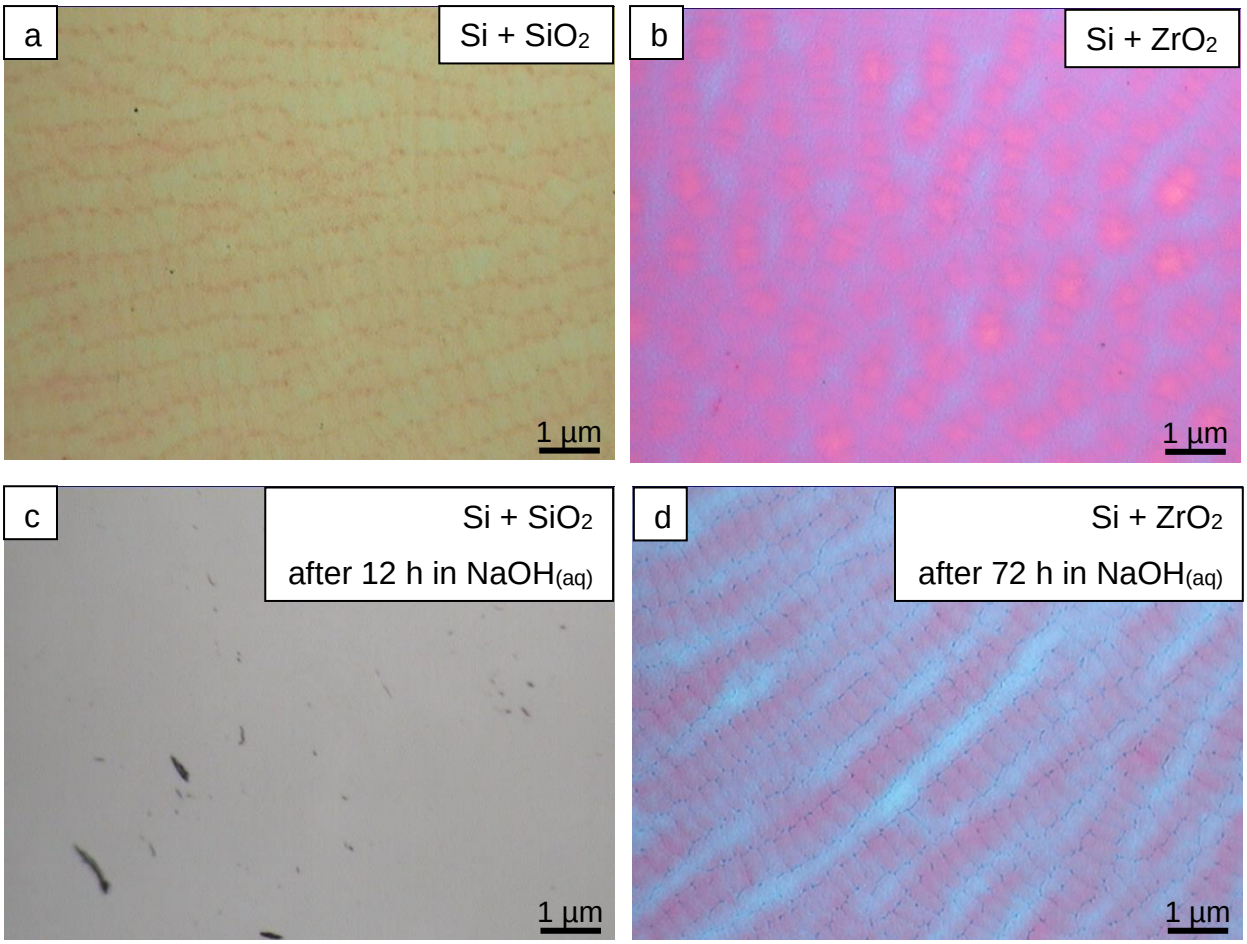

Figure 31: Microscopic images before NaOH treatment of (a) SiO_2 and (b) ZrO_2 as well as after NaOH treatment of (c) SiO_2 and (d) ZrO_2.

The microscopic image of the Si-substrate with the SiO_2-coating shows a certain colour and a distinct structure. Both are no longer visible after placing this sample in an aqueous solution of 0.01 M NaOH for 12 h. With this treatment the coating was completely removed.

For the Si-substrate with the ZrO_2-coating a different colour and structure are observed. After placing the sample in an aqueous solution of NaOH for 72 h the structure is still visible, however, the colour was altered. This could be caused by a change in the optical properties or the electronic as well as the chemical structure of the ZrO_2-coating.

IR spectra of the coatings before and after placing the samples in the aqueous NaOH solution were collected using a FTIR microscope in reflection mode in ambient atmosphere. The spectra are displayed in *Figure 32*.

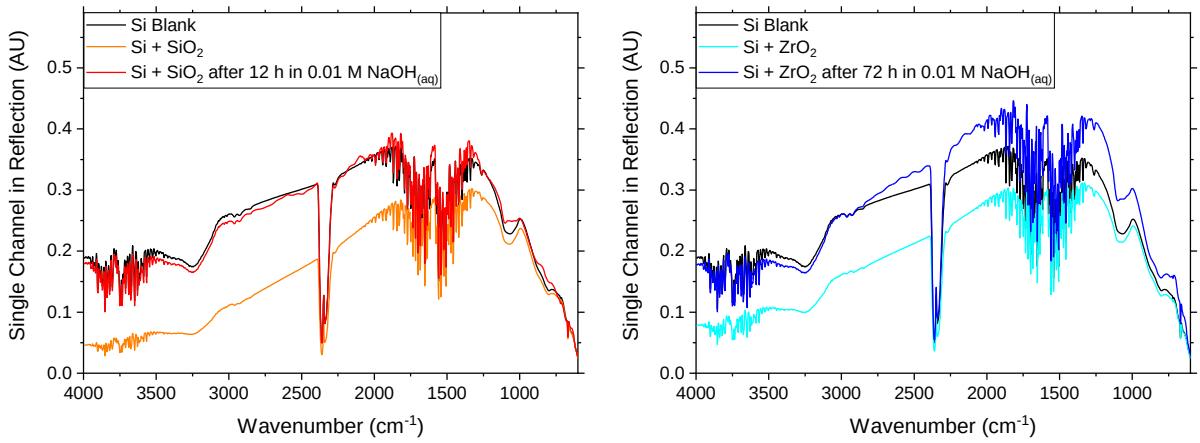

Figure 32: FTIR single channel spectra collected in reflection mode before and after NaOH treatment for the (a) SiO_2- and the (b) ZrO_2-coating.

Si-substrates with the SiO_2- and the ZrO_2-coating show a lower intensity than the blank Si-wafer. It is peculiar that the SiO band at 1075 cm^{-1} of the SiO_2-coating shows a very low absorption. Considering the ATR-FTIR spectrum in *Figure 23a* of the same coating on a Si-ATR crystal, a higher absorption of the SiO stretching vibration would be expected. In reflection mode, the IR beam is focussed on the sample at a certain angle. In reflection absorption experiments the phase change of the incident radiation can cause destructive interference at the surface of the metal, where the reflection takes place. Thus, the resulting intensity of the electric field at the surface is zero and films thinner than the wavelength of the radiation cannot interact with the electric field of the incident radiation. This prevents the absorption of any light [1].

Therefore, the situation of the reflection measurements of these films is more complicated than expected and will not be used for the evaluation. From the spectra, only a difference for both coatings before and after treatment in aqueous 0.01 M NaOH solution is evident.

Additionally, XRD analysis of the coatings before and after the NaOH treatment was performed. The diffraction patterns are displayed in *Figure 33*.

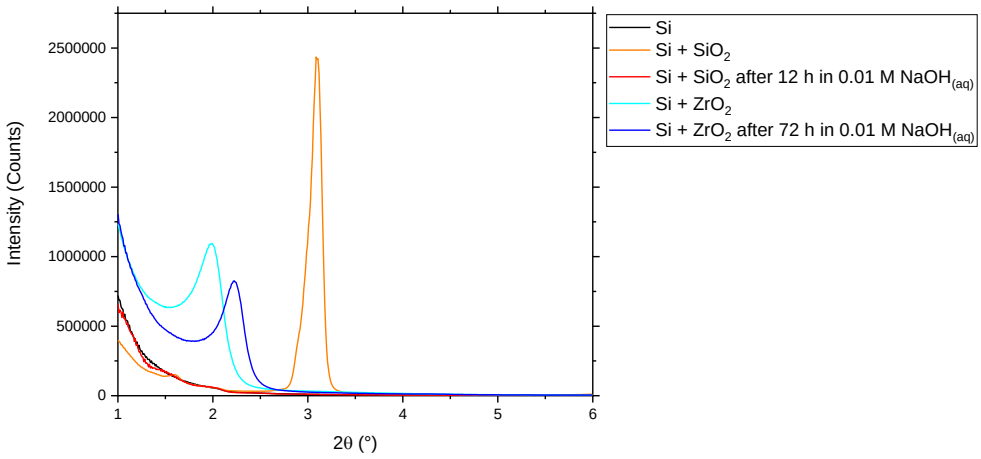

Figure 33: XRD patterns of the SiO_2- and ZrO_2-coating before and after NaOH treatment.

The Si-wafer with the SiO_2-coating shows an intense diffraction peak indicating a highly ordered mesostructure. After placing this sample in the aqueous 0.01 M NaOH solution, the diffraction pattern is almost identical to the uncoated Si-substrate. Thus, the degradation of the mesoporous structure is evident.

The diffraction peak of the ZrO_2-coating shows a shift to higher diffraction angles after the treatment in the aqueous NaOH solution. The calculated areas of both diffraction peaks only differ by 2 %. The contraction calculated from the d-spacings is 10 % [59, 60]. Therefore, the mesoporous ZrO_2-coating is still present, but with a contracted mesostructure. At pH-values above 8.5, the ZrO_2 surface is negatively charged caused by the deprotonation of free OH-groups [83, 84], which could possibly lead to a stronger interaction between free oxygen ions and the Lewis acid sites in ZrO_2. However, further studies are needed to determine the cause for this contraction.

Conclusion

Mesoporous ZrO_2-coatings on wafers and ATR crystals of Si and Ge were prepared successfully. The influence of the chemical composition was investigated. Higher amounts of HCl in the precursor solution result in a reduced thermal stability and decreased diffraction peak intensity associated with the mesostructure.

The influence of the temperature treatment after spin coating on the mesostructure was investigated and an optimised process developed. Ageing the coated substrate for 2 h at ambient temperature, then 1 d at 60°C and finally at 110°C, 150°C and 185°C for 2 d each, leads to highest diffraction peak intensity associated with a mesostructure.

The impact of the relative humidity during spin coating was studied. It shows a strong influence on the measured diffraction peak intensity. For the lowest and highest amount of HCl in the precursor solution, a maximum in diffraction peak intensity is obtained at a relative humidity of 50 % and 35 %, respectively.

FTIR analysis after the ageing process shows that the surfactant is still present in the coatings. Removal by solvent extraction damages the coating, however, calcination at 500°C completely removes the surfactant. In addition, a phase transformation from a 2D hexagonal to a cubic mesostructure is observed in the GI-SAXS patterns.

The temperature stability of coatings was investigated. The L_RH 50 %-coating shows a higher thermal stability compared to the H_RH 35 %-coating. Only the former has a mesostructure after 900°C and shows less recrystallisation than the latter. Additionally, the L_RH 50 %-coating shows a high stability when calcined at 500°C for several hours.

The film thickness of three different Si-wafers with the L_RH 50 %-coating after the ageing process are very similar indicating a high repeatability of the spin coating process. The deviation of the spatial distribution of single coatings is between 2 % and 3 % and were thus neglected for further comparisons. Additionally, both the L_RH 50 %- and the H_RH 35 %-coating show a similar average film thickness before and after calcination at 500°C.

Vibrations of tetragonal and monoclinic ZrO_2 are found in the Raman spectrum of the L_RH 50 %-coating corresponding to the respective symmetry in the coating.

ZrO_2-coated Ge-wafers and ATR crystals show XRD patterns, film thicknesses and FTIR spectra, which are similar to the Si-coated equivalents.

The chemical stability of the ZrO_2-coating in aqueous NaOH solution is confirmed by microscopic images and XRD analysis. The cause of the contraction after placing the ZrO_2-coating in the aqueous NaOH solution still needs further investigation.

4. Surface modification of ZrO_2

Several tests to chemically modify the OH-groups of the ZrO_2-coating were conducted, however, only the following procedure led to a successful modification of the ZrO_2-surface. This process was adapted from literature [85, 86]. Triethoxy(octyl)silane, chlorotrimethylsilane and trichloro(phenyl)silane were used for the surface modification. The ZrO_2-coatings will be named ZrO_2-$Si(CH_2)_7CH_3$, ZrO_2-$Si(CH_3)_3$ and ZrO_2-$Si(C_6H_6)$ for the octyl-, methyl- and phenyl-modified ZrO_2, respectively.

The ZrO_2-coated Si-ATR substrate was ultrasonically cleaned in acetone, EtOH and deionised H_2O for 10 min each. After purging the sample with dry air, the coating was pre-treated at 110°C for approximately 12 h. Then, it was placed in a 3-neck round bottom flask with a reflux condenser and bubbler, N_2-inlet and a vacuum connection. The coating was dried *in vacuo* at 150°C for 2 h. After purging the flask with N_2, 20 mL of $CHCl_3$ and 400 µL of the respective silane were added at ambient temperature. The reaction mixture was kept in inert atmosphere for 24 h. Then, the solution was removed and the ZrO_2-coated substrate ultrasonically cleaned in acetone, EtOH and deionised H_2O for 10 min each. After purging the sample with dry air, the coating was placed in the oven at 90°C for approximately 12 h.

The modified coatings on Si-ATR crystals were analysed using FTIR spectroscopy and the corresponding absorbance spectra are displayed in *Figure 34*.

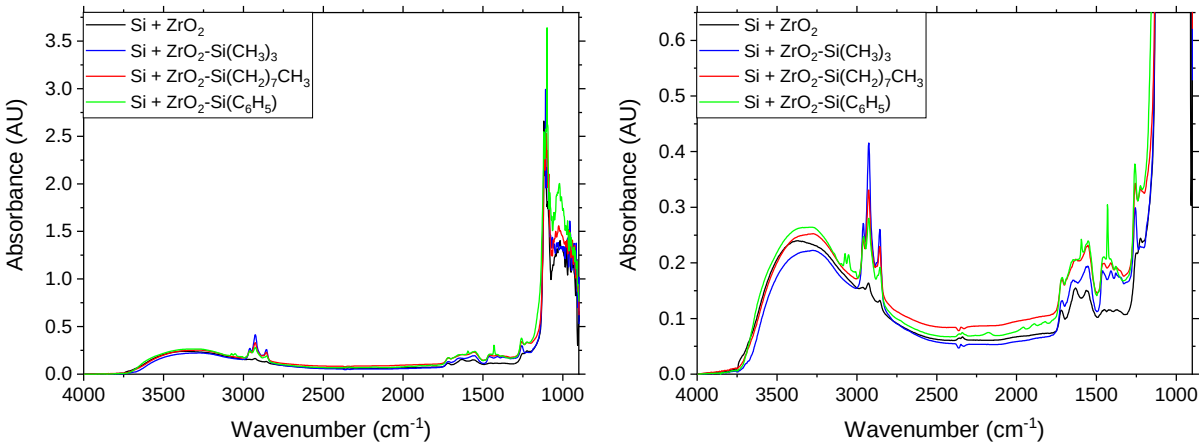

Figure 34: FTIR absorbance spectra of ZrO_2-coated Si-ATR crystals before and after surface modifications.

After the surface modifications bands between 3100 cm^{-1} and 2800 cm^{-1} and bands at about 1250 cm^{-1} can be assigned to stretching and bending vibrations of CH groups, respectively [49]. For the ZrO_2-coating modified with phenyl moieties, bands at 1595 cm^{-1} and 1430 cm^{-1} are characteristic CC stretching vibrations of the benzene ring and for in-plane hydrogen bending, respectively [87, 88].

The band at 1118 cm^{-1} is still present after the functionalisation. Interestingly, the intensity of this band was not increased, even though ZrOSi bonds were introduced into the coating as seen in *Figure 35*. Therefore, it may be concluded that neither surface ZrO-groups nor SiO-vibrations of the Si-ATR crystals cause this band. Instead, they may be attributed to vibrations of the bulk or the interface of the coating and the substrate. Sharp bands around 1100 cm^{-1} appear after functionalisation, which are probably caused by SiO vibrations.

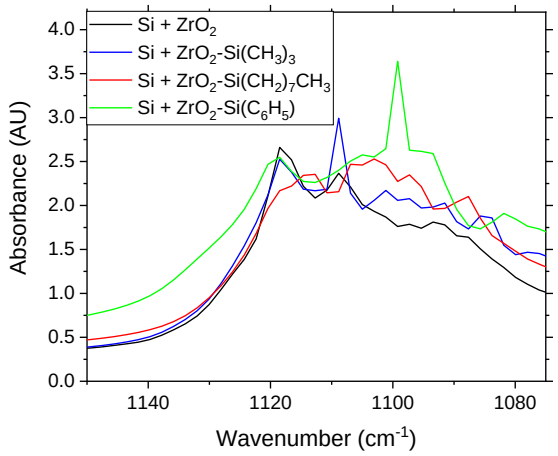

Figure 35: FTIR absorbance spectra of ZrO_2-coated Si-ATR crystals before and after surface modifications between 1150 cm^{-1} and 1075 cm^{-1}.

XRD measurements were conducted to confirm the presence of the mesostructured system after the surface modification. The XRD patterns are displayed in *Figure 36*.

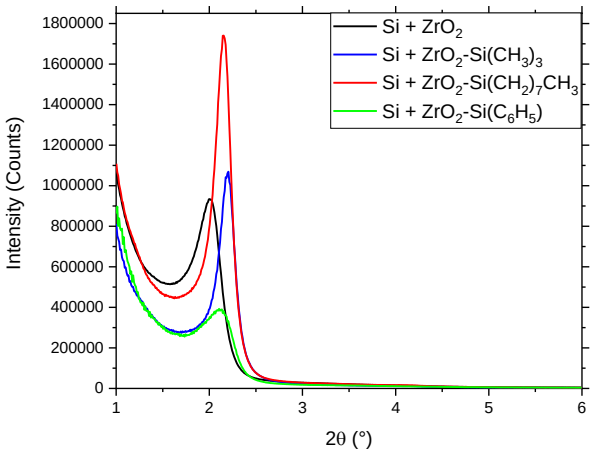

Figure 36: XRD patterns of ZrO_2-coated Si-ATR crystals before and after surface modifications.

The modification process shifts the position of the diffraction peaks to higher 2θ. Compared to the pristine ZrO_2-coating, the functionalisation with octyl moieties shows an increased intensity and area of the diffraction peak. The area of the diffraction peak decreases slightly for the methyl and strongly for the phenyl modification.

This either indicates a damage of the coating upon modifying with phenyl moieties or a distortion in the network reducing the ordering of the mesopores. However, the FTIR spectra in *Figure 34* show no evidence to support the former. In general, all ZrO_2-coated Si-ATR crystals show a mesostructure after the surface modification.

Contact angle measurements of Si-ATR crystals coated with ZrO_2 before and after surface modifications were conducted. The results are displayed in *Figure 37*.

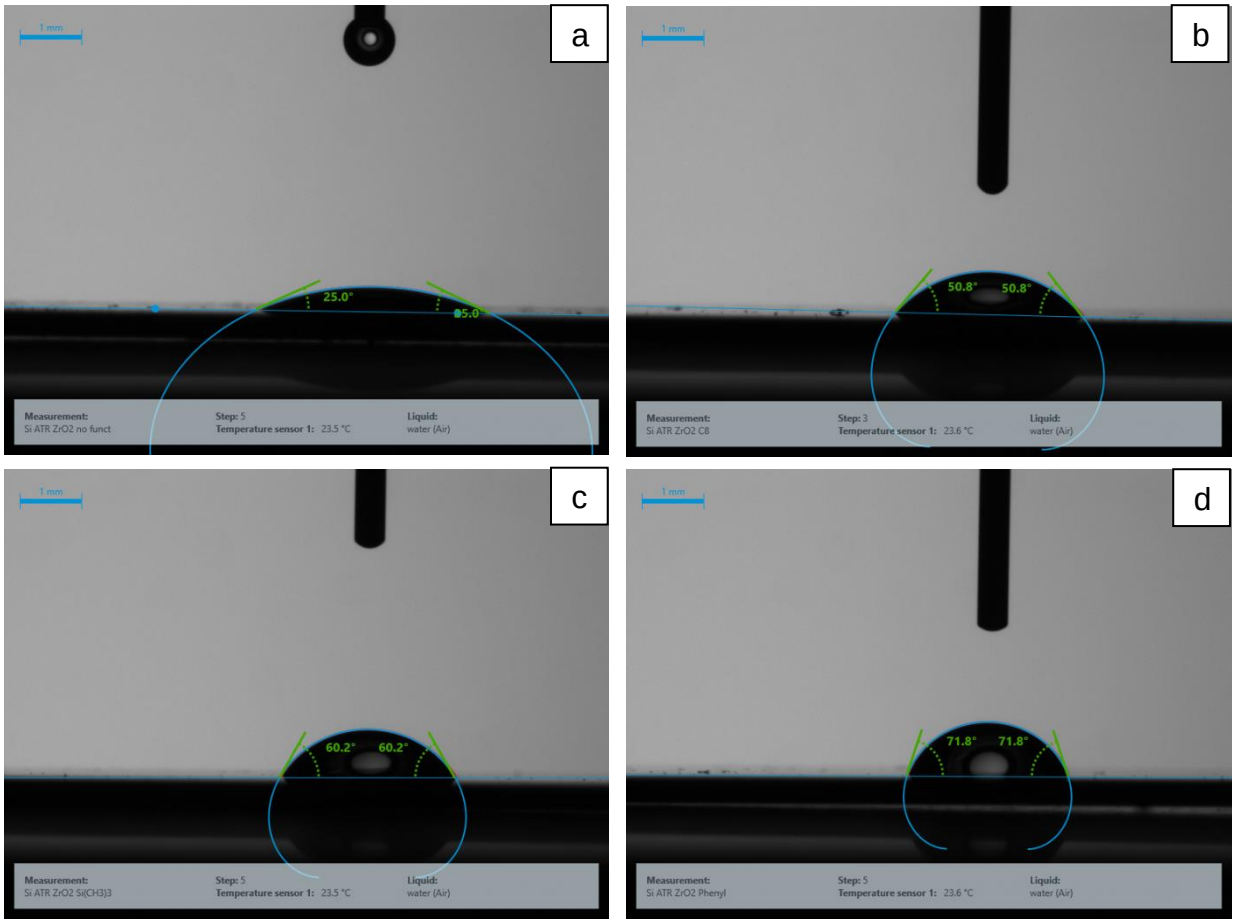

Figure 37: Contact angle measurements of ZrO_2-coated Si-ATR crystals (a) before and after surface modifications with (b) octyl, (c) methyl and (d) phenyl moeities.

The pristine ZrO_2-coating shows a contact angle of 25° indicating a highly hydrophilic surface. Upon introducing octyl moieties, the contact angle reaches a value of 50.8°. For the modification with methyl groups, the contact angle increases to 60.2°. When introducing phenyl moieties, the contact angle reaches a value of 71.8° showing the highest hydrophobicity of these three surface modifications.

Conclusion

Surface modification of ZrO_2 using different silanes was successfully performed. XRD analysis confirms the existence of mesostructures after functionalisation. The presence of the prepared octyl, methyl and phenyl-moieties as well as the ZrO_2-backbone are proven by their FTIR spectra. Additionally, the increase in hydrophobicity compared to the pristine ZrO_2-coating can be seen in contact angle measurements.

5. Enrichment studies

Enrichment studies were performed using the ZrO_2-coated Si- and Ge-ATR crystals and the FTIR setup described in section 2.1. In this chapter, the modified ZrO_2-coatings will be written as ZrO_2-Si$(CH_2)_7CH_3$, ZrO_2-Si$(CH_3)_3$ and ZrO_2-Si(C_6H_5) for the octyl-, methyl- and the phenyl-modification, respectively.

5.1. Proof of principle

Benzonitrile (C_6H_5CN) and valeronitrile (C_4H_9CN) were chosen as model analytes as their CN bands absorb between 2260 cm^{-1} and 2200 cm^{-1} [49], which coincides with the region of highest transmission for Si and show no spectral interferences with the atmosphere. For C_6H_5CN the CN band was integrated between 2260 cm^{-1} and 2210 cm^{-1} and for C_4H_9CN the CN band was integrated between 2275 cm^{-1} and 2225 cm^{-1}.

The single channel spectra of a Si-ATR crystal and a ZrO_2-coated Si-ATR crystal are displayed in *Figure 38*. They grey area visualises the aforementioned region.

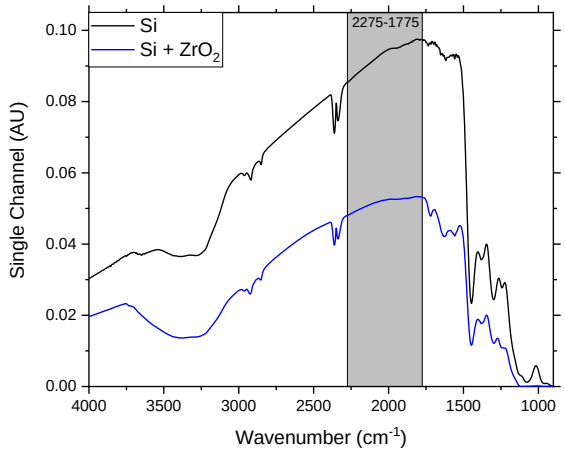

Figure 38: FTIR single channel spectra of an uncoated and ZrO_2-coated Si-ATR crystal.

First, the absorbance of a 4000 mg L^{-1} solution of C_6H_5CN in H_2O was measured using an uncoated and a ZrO_2-coated Si-ATR crystal. The collected absorbance spectra and the calculated area of the CN band of this solution are displayed in *Figure 39*.

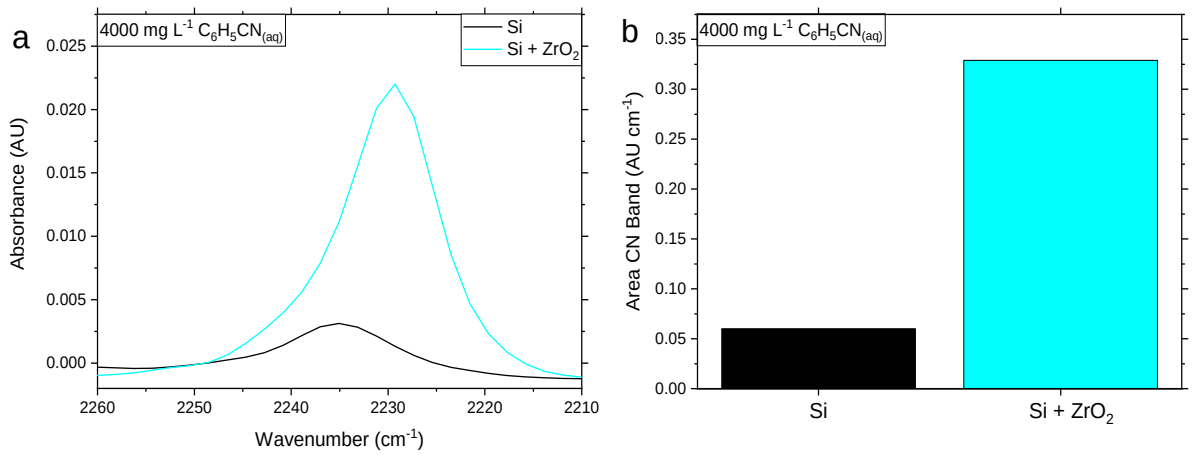

Figure 39: (a) FTIR absorbance spectra of a 4000 mg L^{-1} $C_6H_5CN_{(aq)}$ solution using an uncoated and a ZrO_2-coated Si-ATR crystal and (b) the calculated area of the CN band.

Using an uncoated Si-ATR crystal, only a weak band of C_6H_5CN is observed. For the ZrO_2-coated Si-ATR crystal, a higher absorbance for the C_6H_5CN solution is obtained. Additionally, a shift of the CN band to lower wavenumbers corresponding to a decrease in bond strength indicates an interaction between the ZrO_2-coating and C_6H_5CN. Thus, even the pristine ZrO_2-coating is capable of enriching C_6H_5CN. The calculated area of the CN band increases from 0.060 AU cm^{-1} for the uncoated Si-ATR crystal to 0.329 AU cm^{-1} for the ZrO_2-coated Si-ATR crystal. Thus, an amplification of the absorbance by a factor of 5.5 is obtained.

For the modified ZrO_2-coatings even lower concentrations of C_6H_5CN were detectable. First, the influence of the flow rate was investigated using the ZrO_2-$Si(CH_3)_3$-coating. A solution of 100 mg L^{-1} C_6H_5CN in H_2O was pumped through the flow cell at a rate of 0.5, 1.0, 1.5 and 2.0 mL min^{-1} for 5 min each. Every 4 s an FTIR absorbance spectrum was collected. After the enrichment the flow cell was flushed with deionised H_2O at the same flow rate.

Figure 40 shows the enrichment of 100 mg L^{-1} C_6H_5CN in H_2O using the ZrO_2-$Si(CH_3)_3$-coating with a flow rate of 0.5 mL min^{-1} and displays the calculated area of the CN band in a timeline.

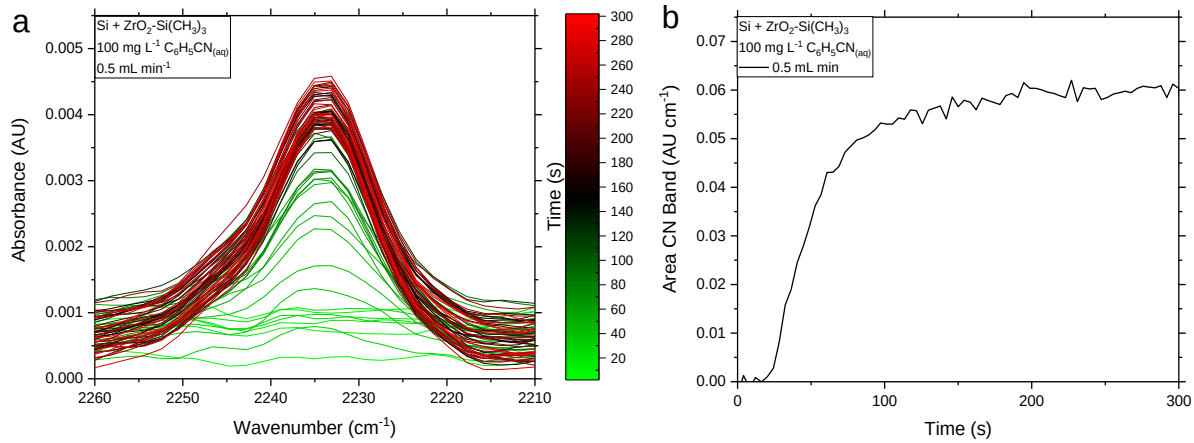

Figure 40: Enrichment of the 100 mg L^{-1} $C_6H_5CN_{(aq)}$ solution using the ZrO_2-$Si(CH_3)_3$-coating at a flow rate of 0.5 mL min^{-1}. (a) FTIR absorbance spectra over time and (b) calculated area of the CN band in a timeline.

The same evaluation was performed for all flow rates. The timelines of the enrichment and the subsequent removal with deionised H_2O of the 100 mg L^{-1} $C_6H_5CN_{(aq)}$ solution at different flow rates are displayed in *Figure 41*.

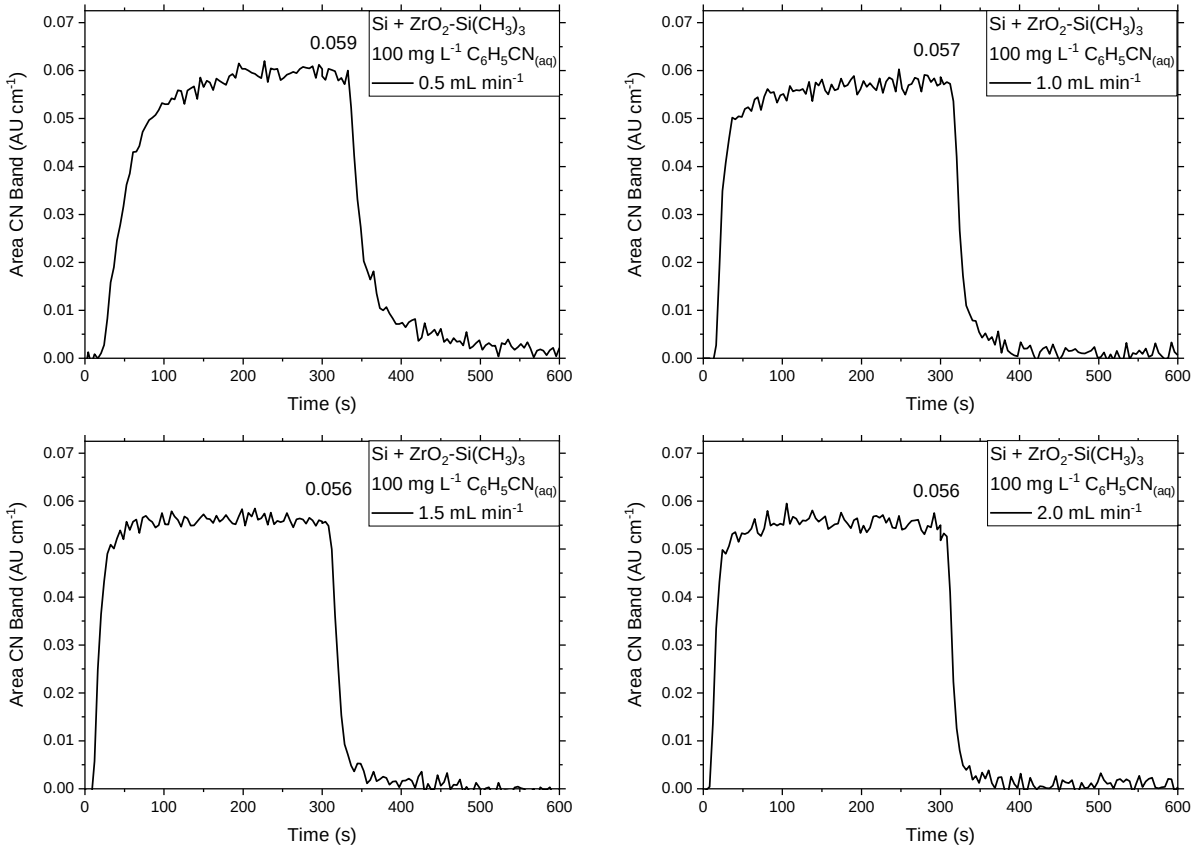

Figure 41: Calculated area of the CN band displayed in a timeline for the enrichment of the 100 mg L^{-1} $C_6H_5CN_{(aq)}$ solution using the ZrO_2-$Si(CH_3)_3$-coating at different flow rates. The corresponding flow rates are displayed in the timelines.

The calculated areas after the complete enrichment of the 100 mg L^{-1} $C_6H_5CN_{(aq)}$ solution only decreases slightly upon increasing the flow rate. However, a faster enrichment and removal of C_6H_5CN is obtained. Additionally, it takes less time for the solution to reach the flow cell. Hence, a flow rate of 2.0 mL min^{-1} was used for all following enrichment studies.

The modified ZrO_2-coatings were used for the enrichment of aqueous C_6H_5CN and C_4H_9CN solutions with concentrations of 10, 25, 50, 75, 100 and 200 mg L^{-1}. The area of the CN band was calculated and the obtained data points fitted by adsorption isotherms. The quality of the fit was evaluated by the χ^2-value. Lower values indicate a better fit for the corresponding model [89].

Typically used models in adsorption processes are Freundlich and Langmuir isotherms. The former assumes a heterogeneous surface with the possibility of multilayer adsorption, however, the latter postulates a uniform surface and only monolayer adsorption [90-92]. The models are expressed by the following equations:

$$q_e = \frac{q_m * K_L * c}{1 + K_L * c} \quad \text{(Eq. 2)}$$

q_e…amount of adsorbed analyte (AU cm^{-1})

q_m…maximum adsorption capacity of the adsorbent (AU cm^{-1})

K_L…Langmuir constant (L mg^{-1})

c…concentration of the analyte in the solution (mg L^{-1})

Equation 2: Adapted Langmuir isotherm taken from ref. [21].

$$q_e = K_F * c^{\frac{1}{n_F}} \quad \text{(Eq. 3)}$$

K_F…Freundlich constant (AU cm^{-1} $[L\ mg]^{1/n_F}$)

n_F…Freundlich linearity index ( )

Equation 3: Adapted Freundlich isotherm taken from ref. [21].

In literature, instead of the concentration of the analyte in the solution (c) the concentration of the solution at equilibrium (C_e) is found [93-95]. The latter is used for discontinuous batch experiments, however, in this experimental setup the flow cell is continuously flushed with analyte solution. Therefore, the concentration of the analyte in the solution was used in *Equation 2* and *Equation 3*.

The calibration curves as well as the fitted isotherms for the enrichment of C_6H_5CN using ZrO_2-coatings with different surface modifications are displayed in *Figure 42*.

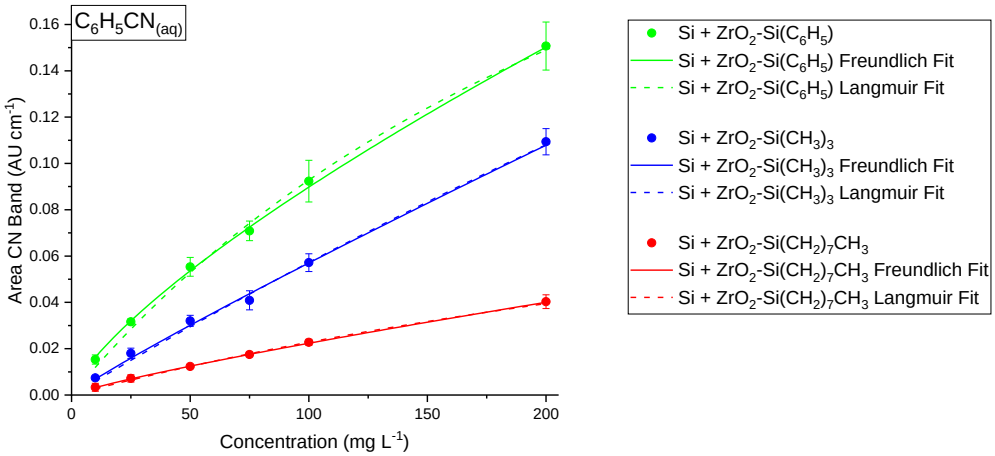

Figure 42: Calibration curves for the enrichment of $C_6H_5CN_{(aq)}$ solutions using ZrO_2-coatings with different surface modifications.

The highest values for the area of the CN band are obtained for the phenyl-modified ZrO_2-coating. The ZrO_2-$Si(CH_2)_7$-coating shows the lowest analyte enrichment. This behaviour correlates with the obtained hydrophobicity from contact angle measurements indicating a higher enrichment of C_6H_5CN for more hydrophobic layers.

The Freundlich fit shows a lower χ^2-value than the Langmuir fit for all coatings used, thus indicating a better fit for this model [89]. The calculated values for χ^2 and the model parameters for the Freundlich fit are summarised in *Table 4*.

Table 4: Calculated χ^2-values for the Freundlich and Langmuir fit as well as the model parameters of the Freundlich fit for the enrichment of C_6H_5CN using ZrO_2-coatings with different surface modifications

Si + ZrO_2-	$\chi^2_{Freundlich}$	$\chi^2_{Langmuir}$	K_F (AU cm^{-1} [L mg^{-1}]$^{1/n_F}$)	n_F
$Si(CH_3)_3$	$6.0\ 10^{-4}$	$1.2\ 10^{-3}$	$8.2\ 10^{-4}$	1.09
$Si(CH_2)_7CH_3$	$1.6\ 10^{-5}$	$2.6\ 10^{-4}$	$4.6\ 10^{-4}$	1.19
$Si(C_6H_5)$	$2.0\ 10^{-4}$	$1.6\ 10^{-3}$	$2.9\ 10^{-3}$	1.35

The enrichment of C_4H_9CN was performed similarly. *Figure 43* shows the enrichment of the 100 mg L^{-1} $C_4H_9CN_{(aq)}$ solution using the ZrO_2-$Si(CH_3)_3$-coating with a flow rate of 2.0 mL min^{-1} and displays the calculated area of the CN band in a timeline.

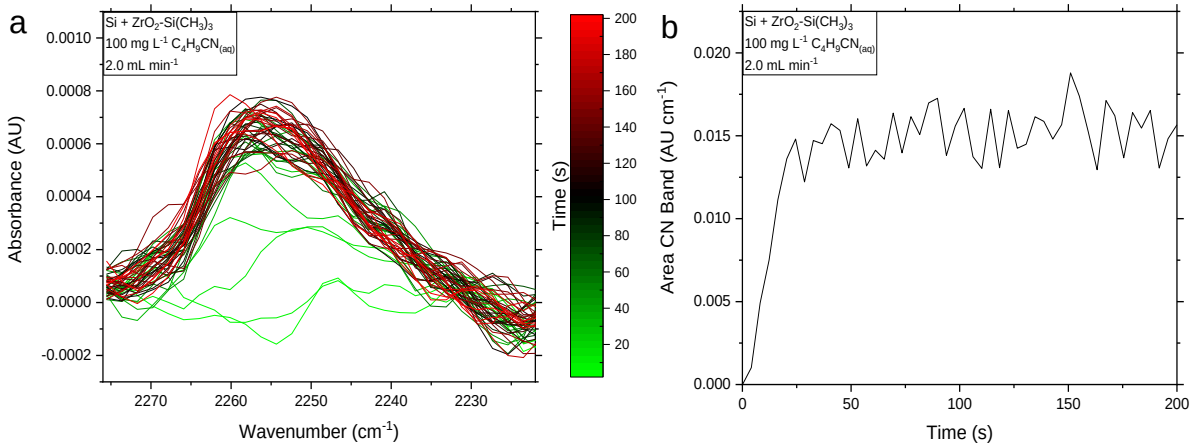

Figure 43: Enrichment of the 100 mg L^{-1} $C_4H_9CN_{(aq)}$ solution using the ZrO_2-$Si(CH_3)_3$-coating at a flow rate of 2.0 mL min^{-1}. (a) FTIR absorbance spectra over time and (b) calculated area of the CN band in a timeline.

The calibration curves as well as the fitted isotherms for the enrichment of C_4H_9CN using ZrO_2-coatings with different surface modifications are displayed in *Figure 44*. No absorbance of the CN bands for the enrichment with the ZrO_2-$Si(CH_2)_7CH_3$-coating are seen. Thus, only the enrichments with the methyl- and phenyl-modified ZrO_2-coating are displayed.

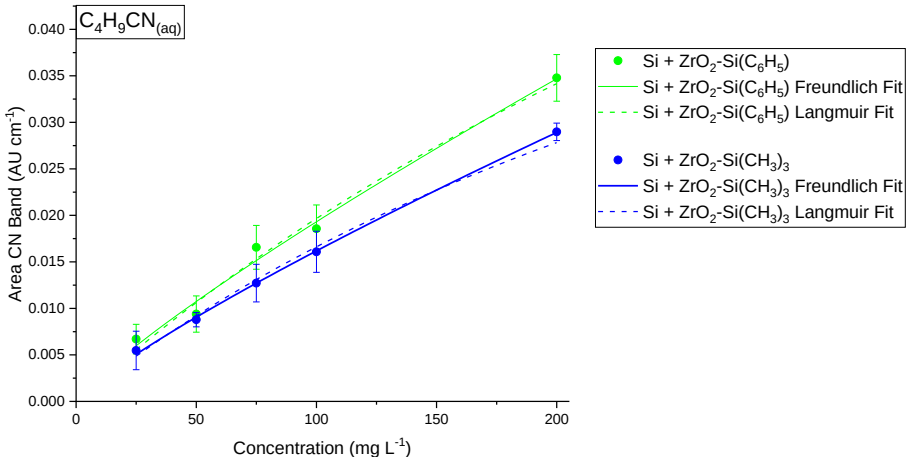

Figure 44: Calibration curves for the enrichment of $C_4H_9CN_{(aq)}$ solutions using ZrO_2-coatings with different surface modifications.

Similar to the enrichment of C_4H_9CN, the highest values for the area of the CN band are obtained for the phenyl-modified ZrO_2-coating. Therefore, this coating shows the highest enrichment for C_4H_9CN. For the octyl-modified ZrO_2-coating, no CN band is observed indicating the poorest enrichment for this coating. Again, this behaviour correlates with the obtained hydrophobicity of the modified ZrO_2-coatings.

The Freundlich fit shows a lower χ^2-value than the Langmuir fit for all coatings used, thus indicating a better fit for this model [89]. The calculated values for χ^2 and the model parameters for the Freundlich fit are summarised in *Table 5*.

Table 5: Calculated χ^2-values for the Freundlich and Langmuir fit as well as the model parameters of the Freundlich fit for the enrichment of C_4H_9CN using ZrO_2-coatings with different surface modifications

Si + ZrO_2-	$\chi^2_{Freundlich}$	$\chi^2_{Langmuir}$	K_F (AU cm^{-1} [L mg^{-1}]$^{1/n_F}$)	n_F
$Si(CH_3)_3$	$4.1\ 10^{-5}$	$1.6\ 10^{-4}$	$3.4\ 10^{-4}$	1.19
$Si(C_6H_5)$	$4.2\ 10^{-4}$	$5.5\ 10^{-4}$	$3.9\ 10^{-4}$	1.18

The obtained calibration curves as well as the fitted isotherms for the enrichment of both analytes C_6H_5CN and C_4H_9CN with the ZrO_2-$Si(C_6H_5)$-coating are displayed in *Figure 45* for comparison.

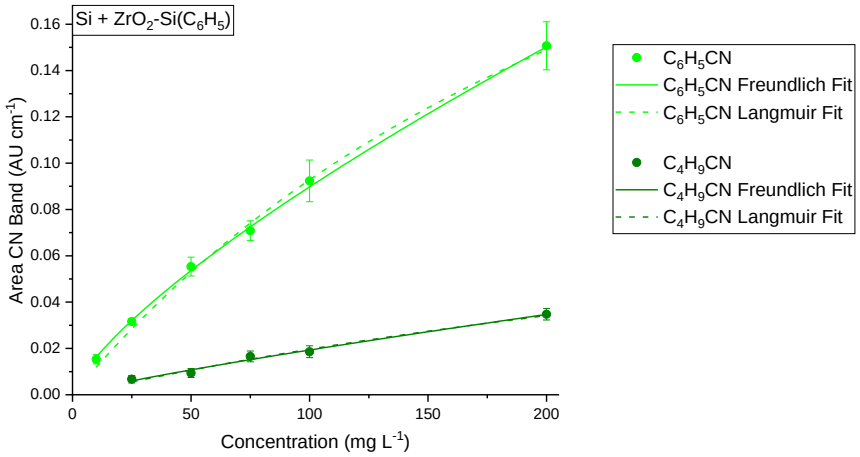

Figure 45: Calibration curves for the enrichment of $C_6H_5CN_{(aq)}$ and $C_4H_9CN_{(aq)}$ solutions using the ZrO_2-$Si(C_6H_5)$-coating.

In *Figure 45* the difference in the enrichment of C_6H_5CN and C_4H_9CN for the phenyl-modified ZrO_2-coating is clearly visible. However, as both analytes differ in molar decadic absorption coefficient and molar weight, a correction of the calculated areas is needed for comparison.

According to literature, the molar decadic absorption coefficients for the CN stretching vibration is 2350 L mol^{-1} cm^{-1} and 1388 L mol^{-1} cm^{-1} for C_6H_5CN and C_4H_9CN, respectively [21]. Using the molar weight of both analytes, mass decadic absorption coefficients of 22.81 L g^{-1} cm^{-1} for C_6H_5CN and 16.70 L g^{-1} cm^{-1} for C_4H_9CN are derived. Thus, for the comparison, the calculated area of the CN band of C_4H_9CN has to be multiplied by the ratio of the mass decadic absorption coefficients of 1.366. However, even after the correction, C_4H_9CN would still show a lower area of the CN band for this coating. This indicates, that the ZrO_2-$Si(C_6H_5)$-coating shows a higher enrichment of C_6H_5CN than C_4H_9CN.

Similarly, the obtained calibration curves as well as the fitted isotherms for the enrichment of C_6H_5CN and C_4H_9CN with the ZrO_2-$Si(CH_3)_3$-coating are displayed in *Figure 46* for comparison.

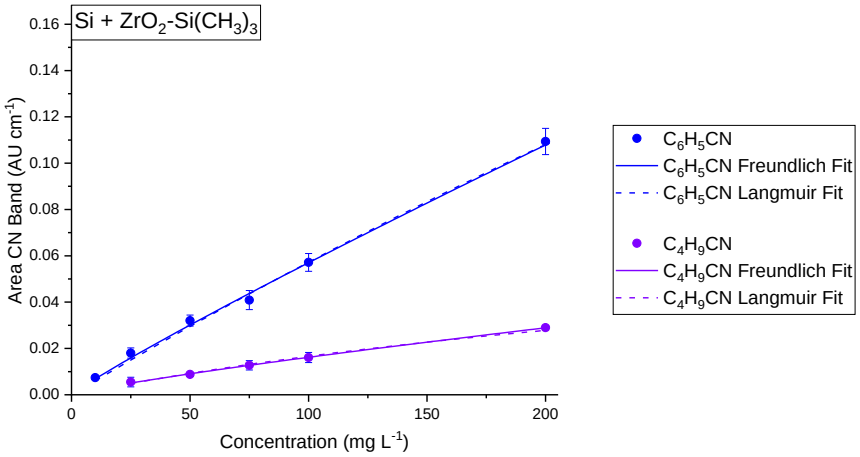

Figure 46: Calibration curves for the enrichment of $C_6H_5CN_{(aq)}$ and $C_4H_9CN_{(aq)}$ solutions using the ZrO_2-$Si(CH_3)_3$-coating.

The results are similar to the enrichment with the phenyl-modified ZrO_2-coating. Again, even after the correction, the area of the CN band of C_4H_9CN would still be lower. However, the distinction between the enrichment of C_6H_5CN and C_4H_9CN is definitely less pronounced for this coating compared to the ZrO_2-$Si(C_6H_5)$-coating.

This shows that all coatings enrich more C_6H_5CN than C_4H_9CN independent of the surface modification. However, to compare the individual modifications, more studies are needed to consider differences in porosity and the amount of functional groups present in the coatings.

5.2. Enrichment of benzene

As the aromatic analyte C_6H_5CN shows a higher enrichment than the aliphatic analyte C_4H_9CN, further enrichment studies with benzene (C_6H_6) were performed. In literature a similar enrichment of C_6H_6 with a methyl-modified mesoporous SiO_2 was reported [50]. Therefore, the enrichment of C_6H_6 was conducted using the ZrO_2-$Si(CH_3)_3$-coating.

As the solutions used for enrichment were pumped from an open volumetric flask into the flow cell, the high volatility of C_6H_6 has to be considered. Therefore, the concentration of C_6H_6 in H_2O was determined using a UV/Vis spectrometer before and after the enrichment. From the absorption at 255 nm the molar concentration was calculated using the Beer-Lambert law and the molar decadic absorption coefficient of 210 L mol^{-1} cm^{-1} [2, 96]. The mass concentration was then calculated using the molar mass of C_6H_6.

The absorbance of the ring mode vibration at 1480 cm^{-1} was used for analysis [97]. The band of the ring mode vibration was integrated between 1490 cm^{-1} and 1470 cm^{-1}. *Figure 47* shows the enrichment of 137 mg L^{-1} C_6H_6 in H_2O using the ZrO_2-$Si(CH_3)_3$-coating with a flow rate of 2.0 mL min^{-1}. Additionally, the calculated area of the ring mode band is displayed in a timeline.

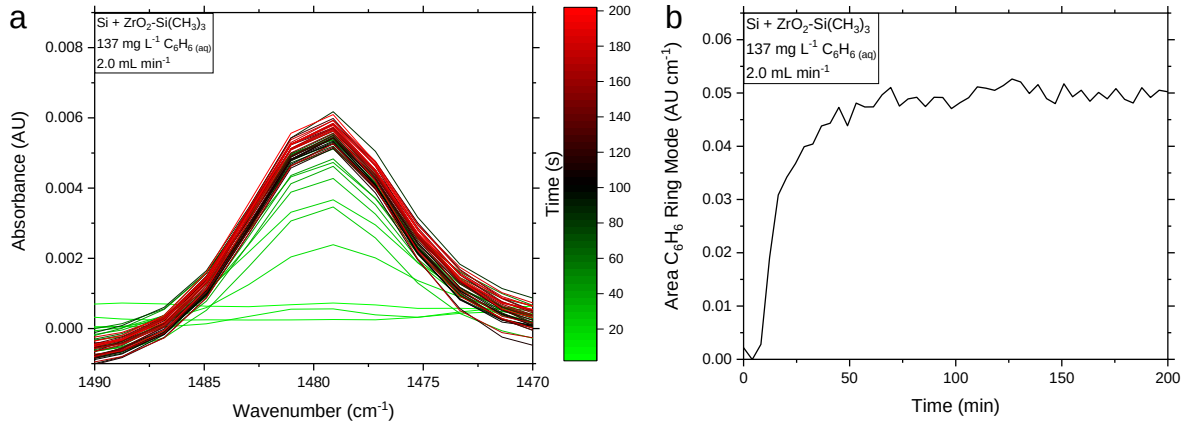

Figure 47: Enrichment of the 137 mg L^{-1} $C_6H_{6\ (aq)}$ solution using the ZrO_2-$Si(CH_3)_3$-coating at a flow rate of 2.0 mL min^{-1}. (a) FTIR absorbance spectra over time and (b) calculated area of the ring mode band in a timeline.

The calibration curve for the enrichment of C_6H_6 with the ZrO_2-$Si(CH_3)_3$-coating is displayed in *Figure 48*.

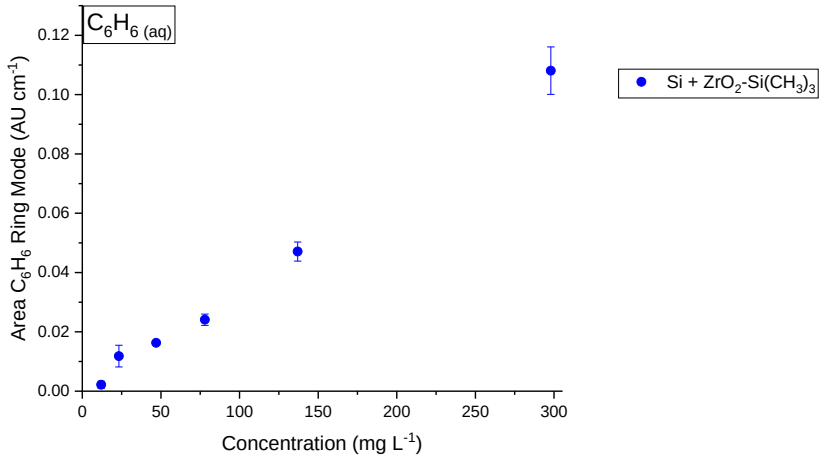

Figure 48: Calibration curve for the enrichment of $C_6H_{6\,(aq)}$ solutions using the ZrO_2-$Si(CH_3)_3$-coating.

The plotted data shows an untypical course for both Langmuir and Freundlich isotherms. However, it may correspond to a BET-isotherm as described in literature [98], but more data is needed to determine if the BET-isotherm is justified for this system.

5.3. Enrichment of ionic species

ZrO_2 is very interesting for chromatographic and catalytic applications, as its surface exhibits acidic, basic, oxidising as well as reducing properties [99, 100]. The surface Zr ions act as strong Lewis acid sites as seen in literature, where interactions with ammonia led to the formation of covalent bonds. Additionally, the basicity of the surface oxygen atoms was confirmed by CO_2 adsorption experiments [61]. From these experiments, the ZrO_2-coating should be capable of enriching both cationic and anionic analytes by interacting with surface oxygen atoms and Zr atoms, respectively.

Therefore, the enrichment of cationic and anionic species using the pristine ZrO_2-coating was studied. For the former, CTAB was used as it is easily detectable by FTIR spectroscopy due to its long alkyl chain. Furthermore, CTAB is a frequently used corrosion inhibitor for steel and, therefore, of great importance in chemical industry [101].

For the enrichment of anionic species KH_2PO_4 was used. Several studies for the removal of phosphate in wastewater were conducted due to its contribution to eutrophication [102-105]. Additionally, a previous study focused on the removal of phosphate using mesoporous ZrO_2 [106]. Another important aspect is that $H_2PO_4^-$ shows prominent absorption bands below 1200 cm^{-1}, thereby necessitating the use of enrichment layers other than mesoporous SiO_2 [107].

5.3.1. Enrichment of CTAB

First, the absorbance of a 0.01 M solution of CTAB in H_2O was measured using an uncoated Si-ATR crystal. The area of CH bands between 2980 cm^{-1} and 2800 cm^{-1} were used for the evaluation. *Figure 49* shows the FTIR absorbance spectra of the enrichment and the calculated areas of the CH bands in a timeline.

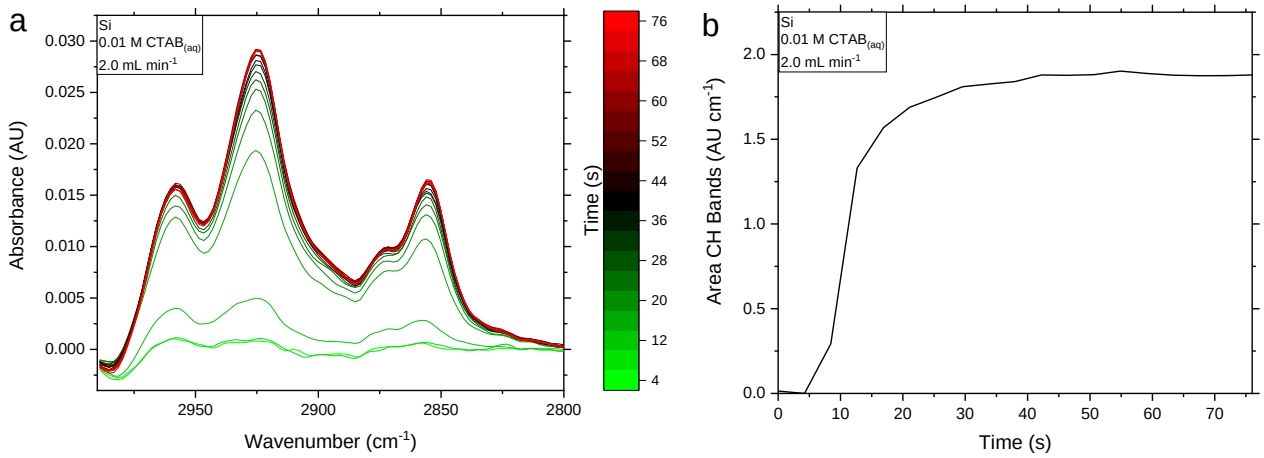

Figure 49: Enrichment of the 0.01 M $CTAB_{(aq)}$ solution using the uncoated Si-ATR crystal at a flow rate of 2.0 mL min^{-1}. (a) FTIR absorbance spectra over time and (b) calculated area of the CH bands in a timeline.

As seen in *Figure 49*, a maximum absorbance is reached after approximately 60 s. The same solution was then applied onto a Si-wafer with a ZrO_2-coating. *Figure 50* shows the enrichment of the 0.01 M solution of CTAB in H_2O with a flow rate of 2.0 mL min^{-1} and displays the calculated area of the CH bands in a timeline.

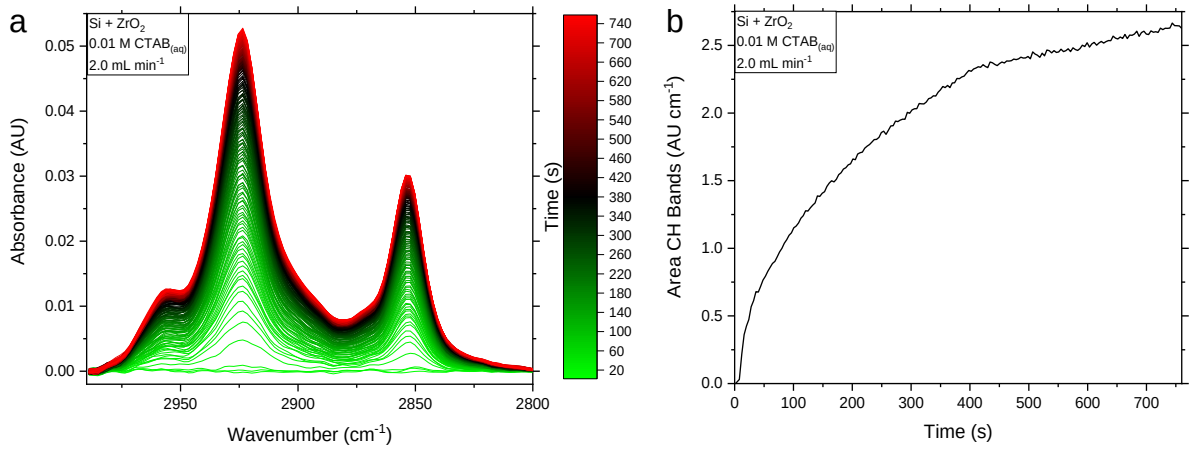

Figure 50: Enrichment of the 0.01 M $CTAB_{(aq)}$ solution using a ZrO_2-coated Si-ATR crystal at a flow rate of 2.0 mL min^{-1}. (a) FTIR absorbance spectra over time and (b) calculated area of the CH bands in a timeline.

The timeline shows a rapid increase at first, which decreases after a few seconds and again after approximately 400 s. However, even after 760 s no maximum absorbance is reached. Compared to the results of the uncoated Si-ATR crystal, the obtained absorbance is higher for the ZrO_2-coated Si-ATR crystal after approximately 270 s of enrichment. For comparison, the FTIR absorbance spectra over time for the enrichment of the 0.01 M $CTAB_{(aq)}$ solution using an uncoated and a ZrO_2-coated Si-ATR crystal are displayed in *Figure 51a* and *Figure 51b*, respectively.

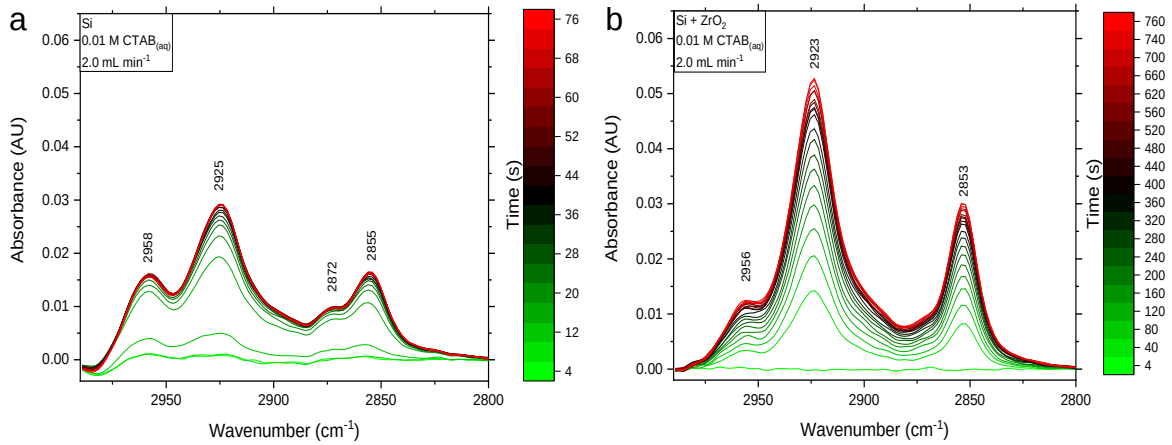

Figure 51: FTIR absorbance spectra over time for the enrichment of the 0.01 M $CTAB_{(aq)}$ solution using (a) an uncoated Si-ATR crystal and (b) a ZrO_2-coated Si-ATR crystal.

The bands at 2958 cm^{-1} and 2872 cm^{-1} in *Figure 51a* are attributed to the asymmetrical and symmetrical CH stretching vibration of the methyl group, respectively. The band at 2925 cm^{-1} can be assigned to the asymmetrical and the band at 2855 cm^{-1} to the symmetrical CH stretching vibration of the methylene groups [108]. For the enrichment using the ZrO_2-coated Si-ATR crystal, these band are shifted to lower wavenumbers due to a decrease in chemical bond strength. This indicates an interaction between the coating and CTAB. Additionally, a decrease in absorbance for the stretching vibrations of the methyl group is found when using the ZrO_2-coated system. During the enrichment, only the absorbance of the stretching vibrations of the methylene groups increases strongly.

In literature, minor shifts of methylene CH stretching vibration frequency between disordered liquid-like films and well-packed crystalline-like films are reported. Additionally, the influence of the crystal forms of n-alkanes on the frequency of methyl stretching CH vibrations is found [109, 110]. However, no explanation for the decrease in absorbance for the methyl CH stretching vibrations as seen in *Figure 51* has been found. Possibly, the interaction between stacked methyl groups in the porous coating hinders the vibration, but no prove is available to confirm this hypothesis. Therefore, more studies are needed to explain this phenomenon.

After the incomplete enrichment, the flow cell was flushed with deionised H_2O to remove CTAB from the coating. *Figure 52* shows the FTIR absorbance spectra and the calculated area of the CH bands in a timeline for the removal of CTAB.

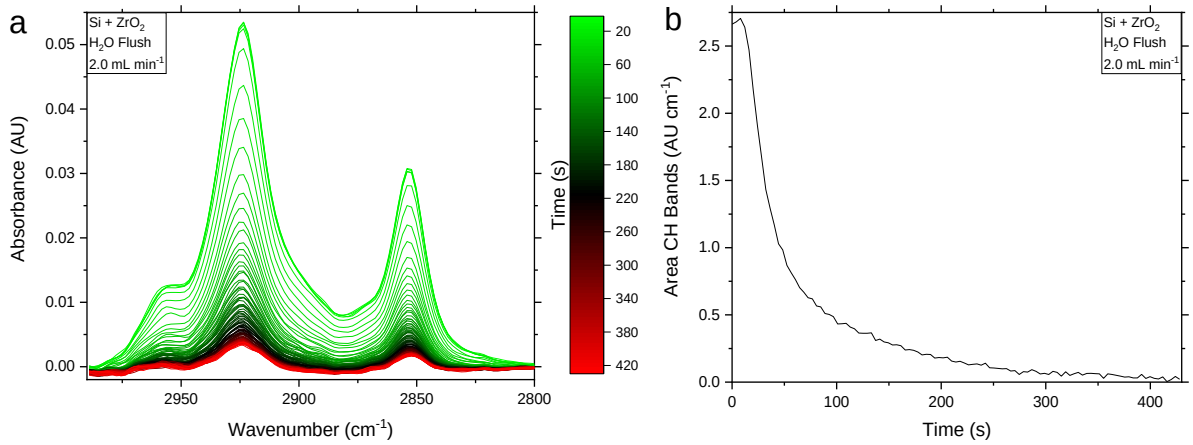

Figure 52: H_2O flush after the enrichment of the 0.01 M $CTAB_{(aq)}$ solution using a ZrO_2-coated Si-ATR crystal at a flow rate of 2.0 mL min^{-1}. (a) FTIR absorbance spectra over time and (b) calculated area of the CH bands in a timeline.

After 300 s the removal of CTAB progresses very slowly and even after 425 s some analyte remains in the ZrO_2-coating as seen in *Figure 52a*.

The results show that the enrichment of the cationic species CTAB with the ZrO_2-coated Si-ATR crystal was successful, but no plateau for the analysed concentration is reached after several minutes prohibiting its application as a sensing device for this concentration range. Additionally, CTAB was not completely removed upon flushing the flow cell with deionised water, which is another reason for its ineptitude as a sensing platform.

Note that further investigations of different cationic species are necessary to study its possible applicability in sensing of cations. However, the experiment showed promising results for the possibility of enriching cationic species.

5.3.2. Enrichment of KH_2PO_4

The affinity of the mesoporous ZrO_2-coating to anionic species was studied using the analyte KH_2PO_4 in H_2O. Ge-ATR crystals, which show a higher transmission at lower wavenumbers, were used instead of Si-ATR crystals. First, Ge-ATR crystals coated with a 20 nm layer of SiO_2 were used, which were already available from another project.

For comparison the FTIR single channel spectra of uncoated and ZrO_2-coated Si- and Ge-SiO_2-ATR crystals are displayed in *Figure 53*.

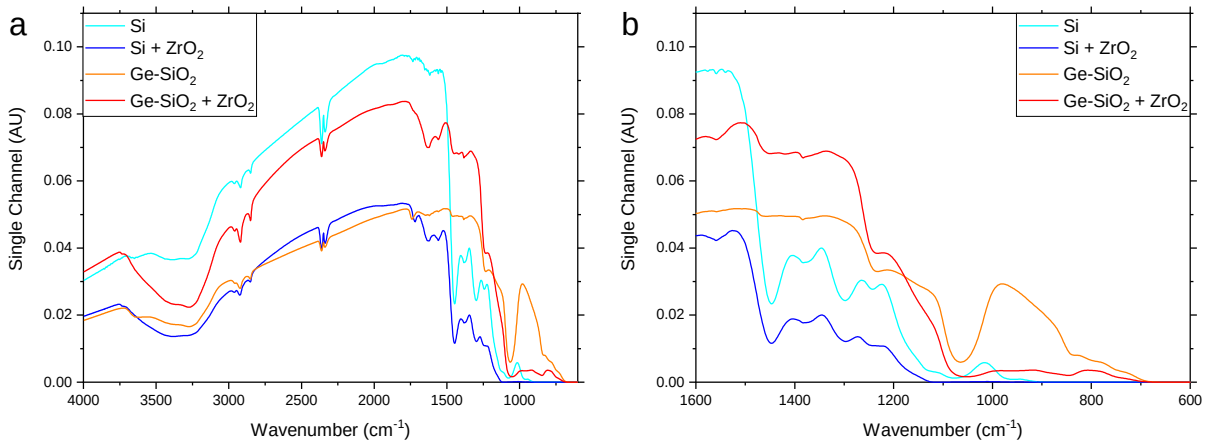

Figure 53: FTIR single channel spectra of uncoated and ZrO_2-coated Si- and Ge-SiO_2-ATR crystals (a) from 4000 cm^{-1} to 600 cm^{-1} and (b) from 1600 cm^{-1} to 600 cm^{-1}.

The uncoated Si-ATR crystal shows almost no signal below 1200 cm^{-1}. After applying the coating, no radiation was transmitted in this region making this system inappropriate for the analysis of $H_2PO_4^-$. The strong absorption band of SiO_2 of the Ge-SiO_2-ATR greatly limits its application for phosphate sensing. The ZrO_2-coating absorbs radiation in this region to some extent, thus further decreasing the signal in the single channel spectrum.

Therefore, new Ge-ATR wafers without the SiO_2-layer were provided by the IMEC research group at Ghent University, polished to ATR crystals and coated with mesoporous ZrO_2. The resulting FTIR single channel spectra are displayed in *Figure 54*.

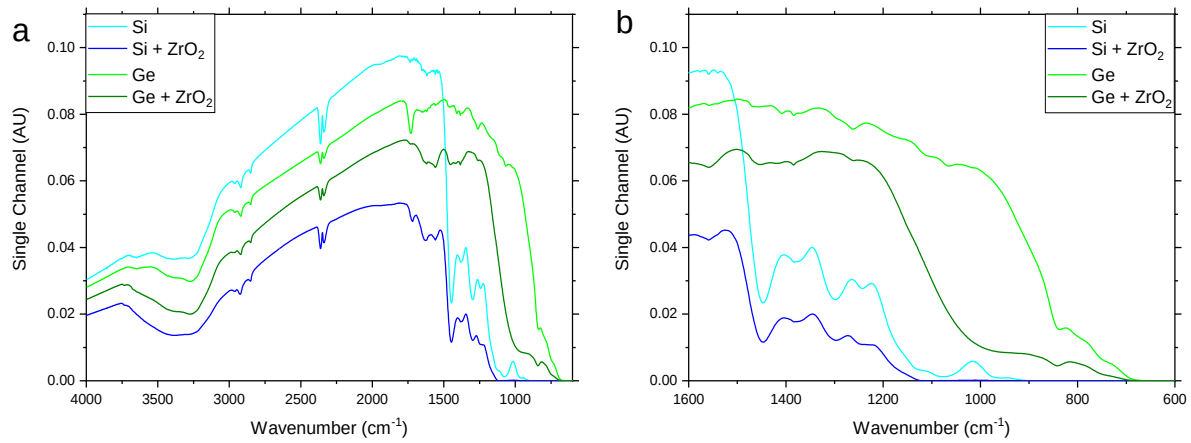

Figure 54: FTIR single channel spectra of uncoated and ZrO_2-coated Si- and Ge- ATR crystals (a) from 4000 cm^{-1} to 600 cm^{-1} and (b) from 1600 cm^{-1} to 600 cm^{-1}.

The new Ge-ATR crystals show less attenuation than Ge-SiO_2-ATR crystals and no band at 1065 cm^{-1} attributed to the SiO stretching vibration. The transmitted signal below 1450 cm^{-1} was higher for the ZrO_2-coated Ge-ATR crystals than for the uncoated and ZrO_2-coated Si-ATR crystals. Therefore, the new ZrO_2-coated Ge-ATR crystals are usable for the enrichment of $H_2PO_4^-$.

First enrichment tests were performed using a ZrO_2-coated Ge-ATR crystal and a solution of 100 mg L^{-1} KH_2PO_4 in H_2O. A flow rate of 2.0 mL min^{-1} was used. The obtained absorbance spectra as well as the timeline of the enrichment are displayed in *Figure 55*.

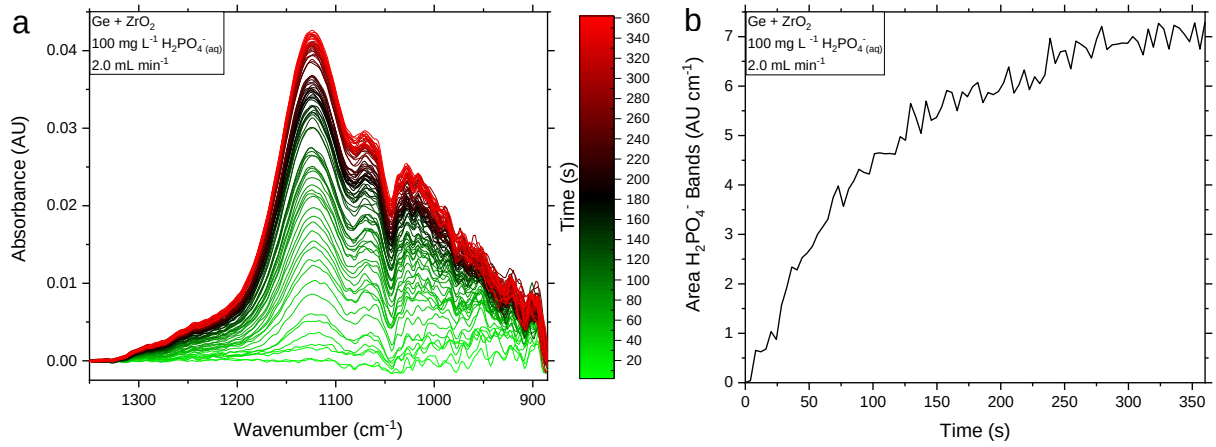

Figure 55: Enrichment of the 100 mg L^{-1} $H_2PO_4^-$(aq) solution using a ZrO_2-coated Ge-ATR crystal at a flow rate of 2.0 mL min^{-1}. (a) FTIR absorbance spectra over time and (b) calculated area of the $H_2PO_4^-$ bands in a timeline.

Figure 55b shows that after 350 s, a maximum in absorbance is reached. After the enrichment, the flow cell was flushed with H_2O for several minutes, where spectra were continuously collected. The FTIR absorbance spectra and the calculated areas of the $H_2PO_4^-$ bands are shown in *Figure 56*.

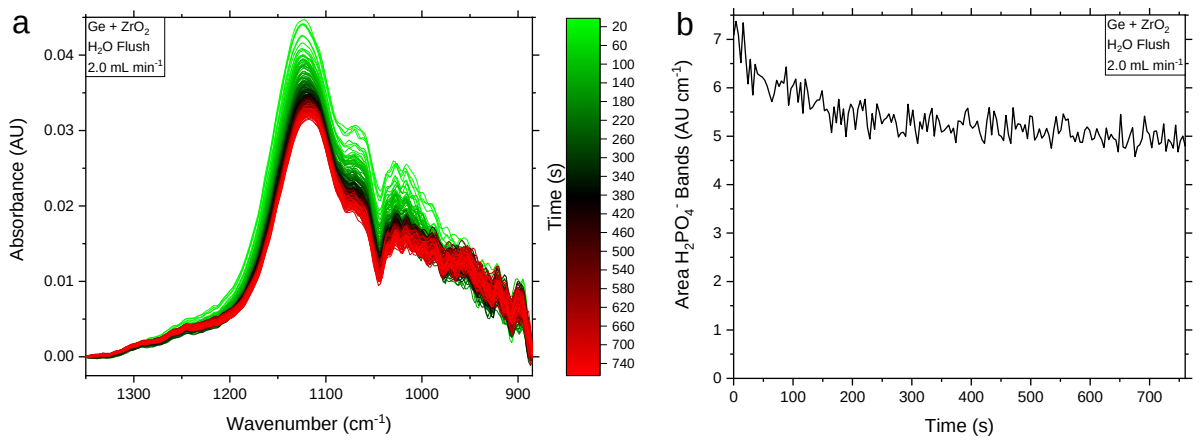

Figure 56: H_2O flush after the enrichment of the 100 mg L^{-1} $H_2PO_4^-{}_{(aq)}$ solution using a ZrO_2-coated Ge-ATR crystal at a flow rate of 2.0 mL min^{-1}. (a) FTIR absorbance spectra over time and (b) calculated area of the $H_2PO_4^-$ bands in a timeline.

Even after 760 s, prominent bands are still visible in the spectrum resulting in a high calculated area. Therefore, H_2O is incapable of removing the analyte from the ZrO_2-coating. Further attempts to remove $H_2PO_4^-$ were conducted. First of all, an aqueous 10^{-3} M NaOH solution was used followed by H_2O. However, this did not suffice to completely remove the analyte from the coating. So an aqueous solution of 1.7 wt% mandelic acid and 8 wt% ammonium citrate was tested, which showed promising results in the dissolution of $Ca_3(PO_4)_2$ in literature [111]. Unfortunately, the subsequent flush with H_2O removes the coating from the Ge-ATR crystal rendering this solution unsuitable.

After the enrichment of the 100 mg L^{-1} $H_2PO_4^-{}_{(aq)}$ solution with a second ZrO_2-coated Ge-ATR crystal , another test to remove the analyte from the coating was conducted using a 0.01 M solution of KCl dissolved in an aqueous 0.1 M NaOH solution as reported in literature [106]. Even though a decrease in absorbance was visible, the analyte was not completely removed. Afterwards, the flow cell was flushed with H_2O, but in this step the ZrO_2-coating was removed from the Ge-ATR crystal.

As the removal of $H_2PO_4^-$ was not possible to this point, enrichments of aqueous KH_2PO_4 solutions with increasing concentrations were conducted. Each concentration step was measured until no visible change in the absorbance spectra was observed. The area was then calculated and summarised in a timeline.

Figure 57 shows the absorbance spectra of the enrichment of $H_2PO_4^-$ as well as a timeline of the calculated areas.

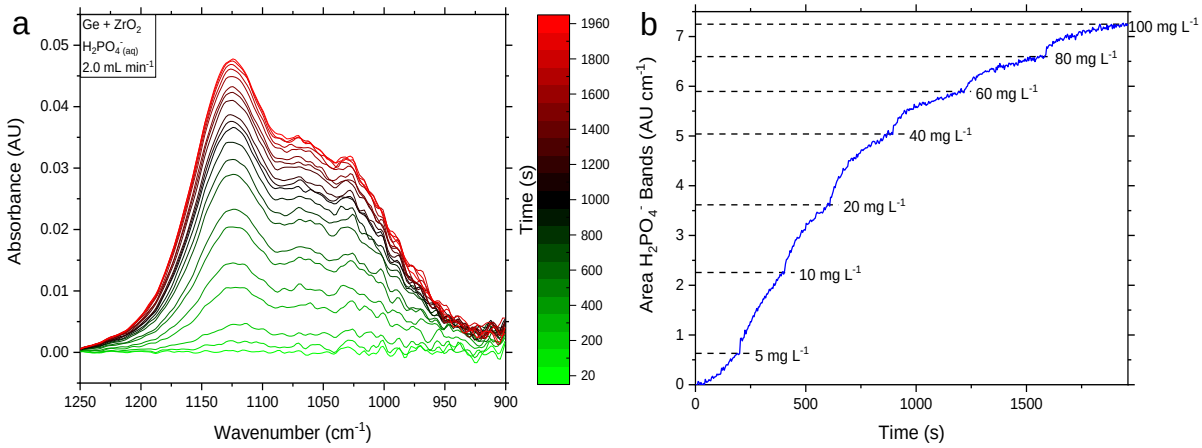

Figure 57: Enrichment of $H_2PO_4^-{}_{(aq)}$ solutions with increasing concentrations using a ZrO_2-coated Ge-ATR crystal at a flow rate of 2.0 mL min^{-1}. (a) FTIR absorbance spectra over time and (b) calculated area of the $H_2PO_4^-$ bands in a timeline.

A lot of time is needed for the enrichment of each concentration step to reach a maximum in absorbance. This greatly limits its application as sensing platform.

The calibration curve as well as the fitted isotherms for the enrichment of $H_2PO_4^-$ using the pristine ZrO_2-coating on a Ge-ATR crystal is displayed in *Figure 58*.

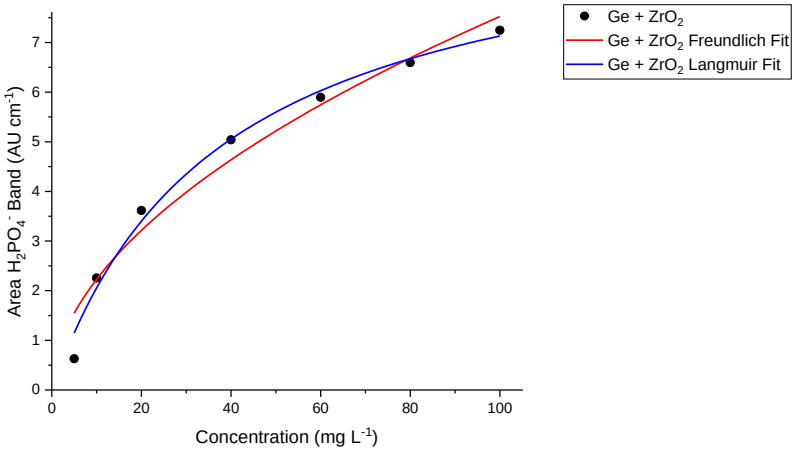

Figure 58: Calibration curve for the enrichment of $H_2PO_4^-{}_{(aq)}$ solutions using the pristine ZrO_2-coating on a Ge-ATR crystal.

The Langmuir fit shows a lower χ^2-value than the Freundlich fit for the enrichment of $H_2PO_4^-$ indicating a better fit for this model [89]. The calculated values for χ^2 and the model parameters for the Langmuir fit are summarised in *Table 6*.

Table 6: Calculated χ^2-values for the Freundlich and Langmuir fit as well as the model parameters of the Langmuir fit for the enrichment of $H_2PO_4^-$ using the pristine ZrO_2-coating on a Ge-ATR crystal

Sample	$\chi^2_{Freundlich}$	$\chi^2_{Langmuir}$	K_L (L mg^{-1})	q_m (AU cm^{-1})
Ge + ZrO_2	0.6406	0.2717	2.649 10^{-2}	98.23

A better fit of the Langmuir isotherm is expected as each ion should occupy just one site on ZrO_2 and the repulsion of the negatively charged $H_2PO_4^-$ ions should prevent the formation of multilayers. The experiments confirmed this hypothesis.

Further studies are needed to design a method capable of removing $H_2PO_4^-$ effectively without damaging the coating. Interestingly, applying the same procedures to a ZrO_2-coated Si-wafer does not remove its coating. Therefore, the interface of the Ge-ATR crystal and the ZrO_2-coating must be the problem.

5.4. Conclusion

Studies were performed using the pristine ZrO_2-coating for the enrichment of the ionic species CTAB and $H_2PO_4^-$, whereas the chemically modified ZrO_2-coatings were used for the enrichment of C_6H_5CN, C_4H_9CN and C_6H_6.

For the enrichment of C_6H_5CN, the influence of the flow rate was investigated. Increasing the flow rate results in a faster enrichment and removal of the analyte without significantly decreasing the obtained maximum absorbance.

The influence of the surface modification for the enrichment of C_6H_5CN and C_4H_9CN was investigated. The phenyl-modified ZrO_2-coating shows the highest and the octyl-modification the lowest enrichment of both the aromatic and aliphatic compound. These result correspond to the obtained hydrophobicity from contact angle measurements. However, more studies are needed to determine the influence of porosity and the amount of functional groups present in the coating. All coatings show a higher enrichment for C_6H_5CN compared to C_4H_9CN.

The obtained data was fitted using Freundlich and Langmuir isotherms. In general, the calibration curves show a better correlation with the Freundlich fit when using the chemically modified ZrO_2-coatings. For C_6H_6, further studies are necessary to determine an appropriate adsorption isotherm. The enrichment of $H_2PO_4^-$ using the pristine ZrO_2-coating demonstrates a better fit for the Langmuir isotherm.

The enrichment of the cationic species CTAB was successful, however, no plateau is reached after several minutes and the analyte could not be completely removed when flushing the flow cell with H_2O. To test the applicability of this coating in sensing of positively charged ions, more studies with different cationic analytes are needed.

For the enrichment studies of $H_2PO_4^-$, the coating was applied onto a Ge-ATR crystal. Promising results were obtained as concentrations of 5 mg mL^{-1} are detectable, however, the removal of the analyte was not possible for the tested solutions. Several solutions were tested, but none managed to completely remove $H_2PO_4^-$from the coating. Instead, the coating on the Ge-ATR crystal was removed with all solutions investigated. Interestingly, Si-ATR crystals with the ZrO_2-coating are persistent against the same solutions. Thus, more studies are necessary to investigate the stability issue with ZrO_2-coated Ge-ATR crystals and to find a method for completely removing $H_2PO_4^-$ from the coating.

6. Summary and Outlook

A mesoporous ZrO_2-coating was successfully prepared on Si- and Ge-wafers as well as ATR crystals. The influence of the chemical composition and spin coating parameters were studied. An optimised ageing process was developed, which led to a maximum in diffraction peak intensity associated with the mesostructure. Measurement of the film thickness showed minor spatial deviations and a high repeatability for single coating procedures.

The surfactant used for synthesis was removed by calcination at 500°C as solvent extraction damaged the coating. The thermal stability of the ZrO_2-coating was confirmed and a change in mesostructuring observed after calcination at 500°C. The chemical stability of the ZrO_2-coating compared to a mesoporous SiO_2-coating in alkaline solution was investigated. The former showed an immense resistance, while the latter experienced decomposition.

The surface of the calcined coatings was successfully modified with octyl, methyl and phenyl moieties. The presence of the mesostructure after functionalisation was confirmed with XRD and FTIR analysis. The phenyl-modified ZrO_2-coating showed a decrease in the diffraction peak intensity of the mesostructure indicating a decrease in ordering of the mesopores. More studies are necessary to determine the amount of functional groups in the coating. Contact angle measurements confirmed the success of the surface modification.

Enrichment studies with pristine and modified ZrO_2-coatings were conducted. The flow rate used showed almost no influence on the adsorbed amount of the analyte. Benzonitrile and valeronitrile were successfully enriched and the obtained calibration curves were fitted using Freundlich isotherms. The phenyl-modified coating showed the highest and the octyl-modified coating the lowest enrichment for both analytes. Benzene was successfully enriched using the methyl-modified ZrO_2-coating. However, the calibration curve could not be fitted using Freundlich or Langmuir isotherms. Further studies are necessary to determine an appropriate model for this enrichment.

CTAB and KH_2PO_4 representing cationic and anionic species, respectively, were successfully enriched using the pristine ZrO_2-coating. However, the enrichment of CTAB showed no plateau, but continuously increased. Additionally, complete removal by flushing with H_2O was not possible. The enrichment of KH_2PO_4 was a very slow and the analyte could not be removed by different solvents and the coating was removed from the Ge-ATR crystal during this process. Therefore, more studies are necessary to determine an optimal process for removing KH_2PO_4 from the coating without damaging it.

7. Appendix

7.1. Raman spectra

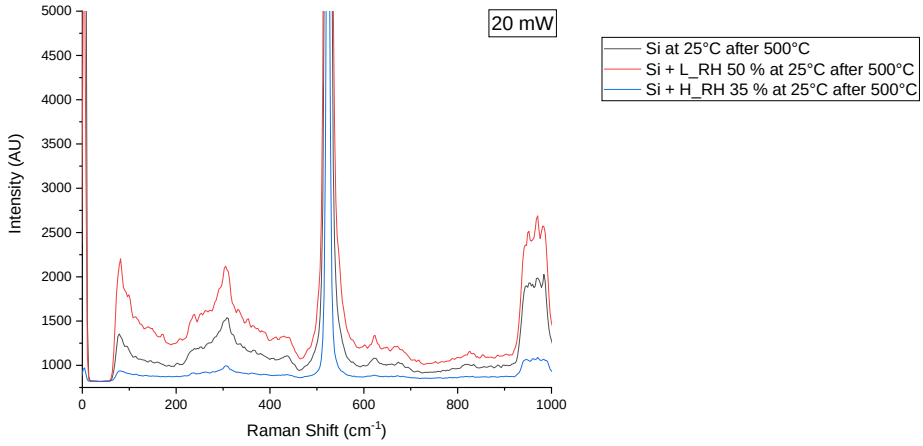

Figure 59: Raman spectra at a laser power of 20 mW of Si with L_RH 50 %-, H_RH 35 %-coating and without coating after calcination at 500°C

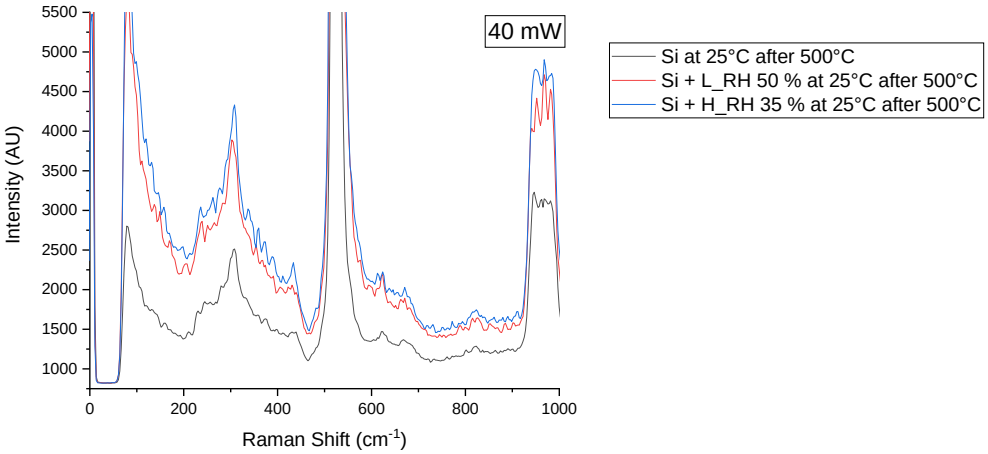

Figure 60: Raman spectra at a laser power of 40 mW of Si with L_RH 50 %-, H_RH 35 %-coating and without coating after calcination at 500°C

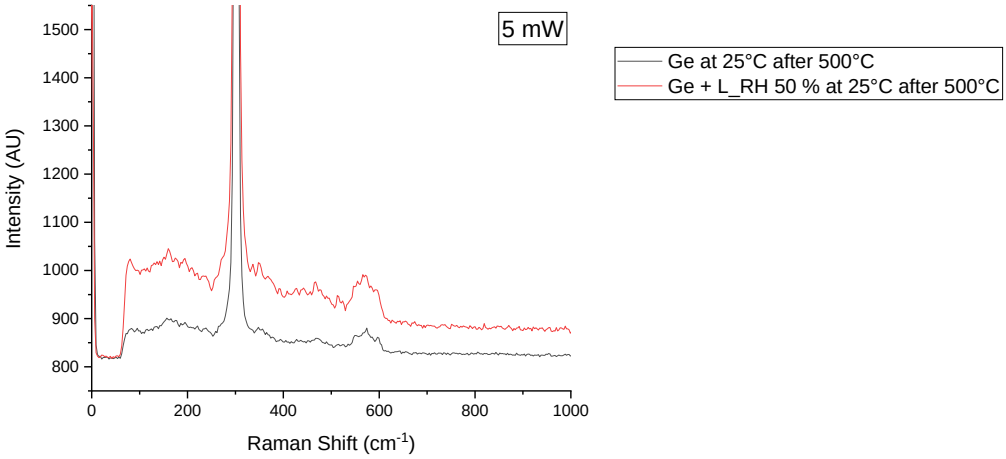

Figure 61: Raman spectra at a laser power of 5 mW of Ge with L_RH 50 %- and without coating after calcination at 500°C

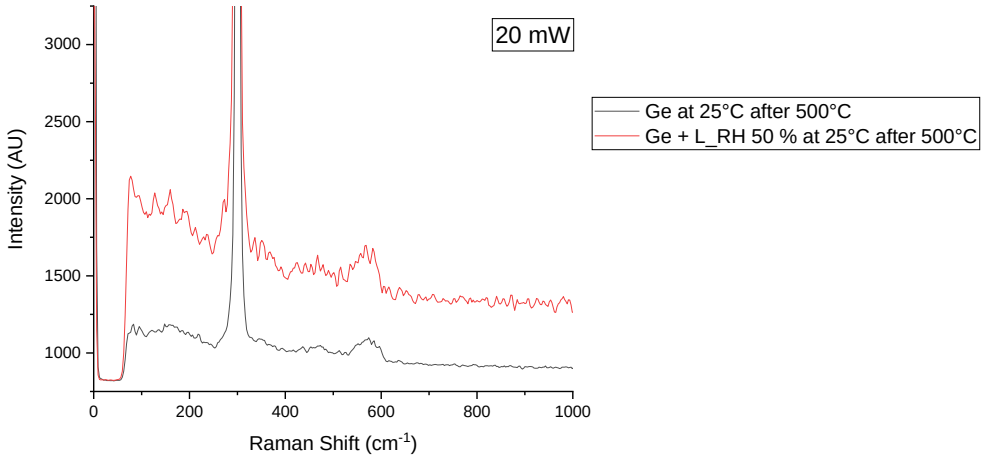

Figure 62: Raman spectra at a laser power of 20 mW of Ge with L_RH 50 %- and without coating after calcination at 500°C

8. References

1. Griffiths, P.R. and J.A. de Haseth, *Fourier Transform Infrared Spectrometry*. 2 ed. 2007, New Jersey: John Wiley & Sons, Inc.
2. Laqua, K., W.H. Melhuish, and M. Zander, *Nomenclature, Symbols, Units and Their Usage in Spectrochemical Analysis .7. Molecular Absorption-Spectroscopy, Ultraviolet and Visible (Uv Vis) - (Recommendations 1988).* Pure and Applied Chemistry, 1988. **60**(9): p. 1449-1460.
3. Fahrenfort, J., *Attenuated Total Reflection - a New Principle for the Production of Useful Infra-Red Reflection Spectra of Organic Compounds.* Spectrochimica Acta, 1961. **17**(7): p. 698-+.
4. Harrick, N.J., *Principles of Internal Reflection Spectroscopy.* Applied Spectroscopy, 1971. **25**(1): p. 142-&.
5. Harrick, N.J., *Internal Reflection Spectra of Semiconductor Surfaces.* Surface Science, 1969. **13**(1): p. 134-&.
6. Mirabella, F.M., *Internal-Reflection Spectroscopy.* Applied Spectroscopy Reviews, 1985. **21**(1-2): p. 45-178.
7. Baird, W.S., et al., *An Automatic Recording Infra-Red Spectrophotometer.* Journal of the Optical Society of America, 1947. **37**(10): p. 754-761.
8. Colthup, N.B., L.H. Daly, and S.E. Wiberley, *Introduction to Infrared and Raman Spectroscopy*. 1964, New York: Academic Press.
9. Milosevic, M., S.L. Berets, and A.Y. Fadeev, *Single-reflection attenuated total reflection of organic monolayers on silicon.* Applied Spectroscopy, 2003. **57**(6): p. 724-727.
10. Milosevic, M., N.J. Harrick, and S.L. Berets, *The Sea-Gull - a Multifunctional Variable-Angle Reflection Attachment.* Applied Spectroscopy, 1991. **45**(1): p. 126-131.
11. Sharpe, L.H., *Observation of Molecular Interactions in Oriented Monolayers by Infrared Spectroscopy Involving Total Internal Reflection.* Proceedings of the Chemical Society of London, 1961(Dec): p. 461-&.
12. Griffiths, P.R., H.J. Sloane, and R.W. Hannah, *Interferometers Vs Monochromators - Separating Optical and Digital Advantages.* Applied Spectroscopy, 1977. **31**(6): p. 485-495.
13. Artyushenko, V., et al., *Mid-IR fibre optics spectroscopy in the 3300-600 cm(-1) range.* Vibrational Spectroscopy, 2008. **48**(2): p. 168-171.
14. Boncheva, M., F. Damien, and V. Normand, *Molecular organization of the lipid matrix in intact Stratum corneum using ATR-FTIR spectroscopy.* Biochimica Et Biophysica Acta-Biomembranes, 2008. **1778**(5): p. 1344-1355.
15. Lumpi, D., et al., *Fibre optic ATR-IR spectroscopy at cryogenic temperatures: in-line reaction monitoring on organolithium compounds.* Chemical Communications, 2012. **48**(18): p. 2451-2453.
16. Doyle, W.M., *Absorbance Linearity and Repeatability in Cylindrical Internal Reflectance Ft-Ir Spectroscopy of Liquids.* Applied Spectroscopy, 1990. **44**(1): p. 50-58.
17. Lamotte, M., et al., *Evaluation of the possibility of detecting benzenic pollutants by direct spectrophotometry on PDMS solid absorbent.* Analytical and Bioanalytical Chemistry, 2002. **372**(1): p. 169-173.
18. Lu, R., et al., *IR-ATR Chemical Sensors Based on Planar Silver Halide Waveguides Coated with an Ethylene/Propylene Copolymer for Detection of Multiple Organic Contaminants in Water.* Angewandte Chemie-International Edition, 2013. **52**(8): p. 2265-2268.
19. Stach, R., et al., *Mid-Infrared Spectroscopic Method for the Identification and Quantification of Dissolved Oil Components in Marine Environments.* Analytical Chemistry, 2015. **87**(24): p. 12306-12312.
20. Baumgartner, B., J. Hayden, and B. Lendl, *Mesoporous silica films for sensing volatile organic compounds using attenuated total reflection spectroscopy.* Sensors and Actuators B-Chemical, 2020. **302**.

21. Baumgartner, B., et al., *In Situ IR Spectroscopy of Mesoporous Silica Films for Monitoring Adsorption Processes and Trace Analysis.* Acs Applied Nano Materials, 2018. **1**(12): p. 7083-7091.
22. Lu, Y.F., et al., *Chemical sensors based on hydrophobic porous sol-gel films and ATR-FTIR spectroscopy.* Sensors and Actuators B-Chemical, 1996. **36**(1-3): p. 517-521.
23. Grahn, M., A. Holmgren, and J. Hedlund, *Adsorption of n-hexane and p-xylene in thin silicalite-1 films studied by FTIR/ATR spectroscopy.* Journal of Physical Chemistry C, 2008. **112**(20): p. 7717-7724.
24. Wang, Z., et al., *Zeolite coated ATR crystals for new applications in FTIR-ATR spectroscopy.* Chemical Communications, 2004(24): p. 2888-2889.
25. Huang, G.G., et al., *ZnO nanoparticle-modified infrared internal reflection elements for selective detection of volatile organic compounds.* Analytical Chemistry, 2006. **78**(7): p. 2397-2404.
26. Innocenzi, P. and L. Malfatti, *Mesoporous thin films: properties and applications.* Chemical Society Reviews, 2013. **42**(9): p. 4198-4216.
27. Soler-Illia, G.J.A.A., et al., *Mesoporous hybrid and nanocomposite thin films. A sol-gel toolbox to create nanoconfined systems with localized chemical properties.* Journal of Sol-Gel Science and Technology, 2011. **57**(3): p. 299-312.
28. Soler-Illia, G.J.D.A., A. Louis, and C. Sanchez, *Synthesis and characterization of mesostructured titania-based materials through evaporation-induced self-assembly.* Chemistry of Materials, 2002. **14**(2): p. 750-759.
29. Bourda, L., et al., *Functionalized periodic mesoporous organosilicas: from metal free catalysis to sensing.* Journal of Materials Chemistry A, 2019. **7**(23): p. 14060-14069.
30. Gibson, L.T., *Mesosilica materials and organic pollutant adsorption: part A removal from air.* Chemical Society Reviews, 2014. **43**(15): p. 5163-5172.
31. Zheng, Q., et al., *Fluoroalcohol and fluorinated-phenol derivatives functionalized mesoporous SBA-15 hybrids: high-performance gas sensing toward nerve agent.* Journal of Materials Chemistry, 2012. **22**(5): p. 2263-2270.
32. Beck, J.S., et al., *A New Family of Mesoporous Molecular-Sieves Prepared with Liquid-Crystal Templates.* Journal of the American Chemical Society, 1992. **114**(27): p. 10834-10843.
33. Kresge, C.T., et al., *Ordered Mesoporous Molecular-Sieves Synthesized by a Liquid-Crystal Template Mechanism.* Nature, 1992. **359**(6397): p. 710-712.
34. Brinker, C.J. and G.W. Scherer, *Sol–gel science, the physics and chemistry of sol–gel processing*. 1990, Boston: Academic Press.
35. Cushing, B.L., V.L. Kolesnichenko, and C.J. O'Connor, *Recent advances in the liquid-phase syntheses of inorganic nanoparticles.* Chemical Reviews, 2004. **104**(9): p. 3893-3946.
36. Ogawa, M., *Formation of Novel Oriented Transparent Films of Layered Silica-Surfactant Nanocomposites.* Journal of the American Chemical Society, 1994. **116**(17): p. 7941-7942.
37. Cagnol, F., et al., *Humidity-controlled mesostructuration in CTAB-templated silica thin film processing. The existence of a modulable steady state.* Journal of Materials Chemistry, 2003. **13**(1): p. 61-66.
38. Grosso, D., et al., *An in situ study of mesostructured CTAB-silica film formation during dip coating using time-resolved SAXS and interferometry measurements.* Chemistry of Materials, 2002. **14**(2): p. 931-939.
39. Grosso, D., et al., *Phase transformation during cubic mesostructured silica film formation.* Chemical Communications, 2002(7): p. 748-749.
40. Ishii, Y., et al., *Pore Size Determination in Ordered Mesoporous Materials Using Powder X-ray Diffraction.* Journal of Physical Chemistry C, 2013. **117**(35): p. 18120-18130.
41. Kruk, M., M. Jaroniec, and A. Sayari, *Adsorption study of surface and structural properties of MCM-41 materials of different pore sizes.* Journal of Physical Chemistry B, 1997. **101**(4): p. 583-589.

42. Ogawa, M. and N. Masukawa, *Preparation of transparent thin films of lamellar, hexagonal and cubic silica-surfactant mesostructured materials by rapid solvent evaporation methods.* Microporous and Mesoporous Materials, 2000. **38**(1): p. 35-41.
43. Besson, S., et al., *Phase diagram for mesoporous CTAB-silica films prepared under dynamic conditions.* Journal of Materials Chemistry, 2003. **13**(2): p. 404-409.
44. Honma, I., et al., *Structural control of surfactant-templated hexagonal, cubic, and lamellar mesoporous silicate thin films prepared by spin-casting.* Advanced Materials, 2000. **12**(20): p. 1529-1533.
45. Zhou, H.S., D. Kundu, and I. Honma, *Synthesis of oriented meso-structure silica functional thin film.* Journal of the European Ceramic Society, 1999. **19**(6-7): p. 1361-1364.
46. Beneitez, N.T., et al., *Mid-IR sensing platform for trace analysis in aqueous solutions based on a germanium-on-silicon waveguide chip with a mesoporous silica coating for analyte enrichment.* Optics Express, 2020. **28**(18): p. 27013-27027.
47. Kawahara, M., H. Nakamura, and T. Nakajima, *Titania and Zirconia - Possible New Ceramic Microparticulates for High-Performance Liquid-Chromatography.* Journal of Chromatography, 1990. **515**: p. 149-158.
48. Wehrli, A., et al., *Influence of Organic-Bases on Stability and Separation Properties of Reversed-Phase Chemically Bonded Silica-Gels.* Journal of Chromatography, 1978. **149**(Feb): p. 199-210.
49. Socrates, G., *Infrared and Raman Characteristic Group Frequencies : Tables and Charts*. 2nd ed. 1994, Chichester ; New York: Wiley. viii, 249 p.
50. Baumgartner, B., *Mid-Infrared Spectroscopy and Porous Oxides: From Trace Analysis to Interactions at Surfaces*, in *Institute of Chemical Technologies and Analytics*. 2019, TU Wien: Vienna.
51. Nishiyama, N., et al., *Enhancement of structural stability of mesoporous silica thin films prepared by spin-coating.* Chemistry of Materials, 2002. **14**(10): p. 4229-4234.
52. Picquart, M., et al., *Dehydration and crystallization process in sol-gel zirconia - Thermal and spectroscopic study.* Journal of Thermal Analysis and Calorimetry, 2004. **76**(3): p. 755-761.
53. Gopalan, R., C.H. Chang, and Y.S. Lin, *Thermal-Stability Improvement on Pore and Phase-Structure of Sol-Gel Derived Zirconia.* Journal of Materials Science, 1995. **30**(12): p. 3075-3081.
54. Kim, J. and Y.S. Lin, *Sol-gel synthesis and characterization of yttria stabilized zirconia membranes.* Journal of Membrane Science, 1998. **139**(1): p. 75-83.
55. Ciesla, U., et al., *Formation of a porous zirconium oxo phosphate with a high surface area by a surfactant-assisted synthesis.* Angewandte Chemie-International Edition in English, 1996. **35**(5): p. 541-543.
56. Wang, K.X., et al., *Thermally stable nanocrystallised mesoporous zirconia thin films.* Microporous and Mesoporous Materials, 2009. **117**(1-2): p. 161-164.
57. Chen, H.R., et al., *A study of novel composite mesoporous zirconia catalyst materials.* Journal of Chemical Engineering of Japan, 2003. **36**(10): p. 1212-1215.
58. Das, S.K., et al., *Self-Assembled Mesoporous Zirconia and Sulfated Zirconia Nanoparticles Synthesized. by Triblock Copolymer as Template.* Journal of Physical Chemistry C, 2009. **113**(20): p. 8918-8923.
59. Bragg, W.H., *The reflection of x-rays by crystals. (II.).* Proceedings of the Royal Society of London Series a-Containing Papers of a Mathematical and Physical Character, 1913. **89**(610): p. 246-248.
60. Dai, M.Z., et al., *Ordered Mesoporous Carbon Composite Films Containing Cobalt Oxide and Vanadia for Electrochemical Applications.* Chemistry of Materials, 2011. **23**(11): p. 2869-2878.
61. Hertl, W., *Surface-Chemistry of Zirconia Polymorphs.* Langmuir, 1989. **5**(1): p. 96-100.
62. Pokrovski, K., K.T. Jung, and A.T. Bell, *Investigation of CO and CO2 adsorption on tetragonal and monoclinic zirconia.* Langmuir, 2001. **17**(14): p. 4297-4303.

63. Bhagwat, M. and V. Ramaswamy, *Synthesis of nanocrystalline zirconia by amorphous citrate route: structural and thermal (HTXRD) studies.* Materials Research Bulletin, 2004. **39**(11): p. 1627-1640.
64. Kasper, J.S. and S.M. Richards, *Crystal Structures of New Forms of Silicon + Germanium.* Acta Crystallographica, 1964. **17**(6): p. 752-&.
65. Peacor, D.R., *High-Temperature Single-Crystal Study of Cristobalite Inversion.* Zeitschrift Fur Kristallographie, 1973. **138**: p. 274-298.
66. Zaslavskii, A.M. and A.V. Melnikov, *Film Structuring in Praseodymium Oxide Zirconium-Oxide and Praseodymium Oxide Hafnium Oxide Systems.* Inorganic Materials, 1993. **29**(2): p. 245-249.
67. Bellakki, M.B., et al., *Synthesis, structure and oxygen-storage capacity of Pr1-xZrxO2-delta and Pr1-x-yPdyZrxO2-delta.* Materials Research Bulletin, 2008. **43**(10): p. 2658-2667.
68. Demuth, T., et al., *Polymorphism in silica studied in the local density and generalized-gradient approximations.* Journal of Physics-Condensed Matter, 1999. **11**(19): p. 3833-3874.
69. Yamaguchi, S., *Ordered Arrangement of Oxygen in Interstitial Solid Solution of Zirconium-Oxygen System.* Journal of the Physical Society of Japan, 1968. **24**(4): p. 855-+.
70. Neris, A.M., et al., *Environmental remediation and synthesis of a new pigment by irradiation-induced adsorption of methylene blue onto undoped tetragonal zirconia.* Materials Letters, 2019. **255**.
71. Yakout, S.M. and H.S. Hassan, *Adsorption Characteristics of Sol Gel-Derived Zirconia for Cesium Ions from Aqueous Solutions.* Molecules, 2014. **19**(7): p. 9160-9172.
72. Zhang, Y., et al., *Arsenate adsorption on an Fe-Ce bimetal oxide adsorbent: Role of surface properties.* Environmental Science & Technology, 2005. **39**(18): p. 7246-7253.
73. Nakamoto, K., *Infrared and Raman Spectra of Inorganic and Coordination Compounds*, in *Handbook of Vibrational Spectroscopy*. 2001.
74. Luo, Y.R., *Comprehensive Handbook of Chemical Bond Energies*. 1 ed. 2007, Boca Raton: CRC Press.
75. Solveyra, E.G., et al., *2D-SAXS In Situ Measurements as a Tool To Study Elusive Mesoporous Phases: The Case of p6mm TiO2.* Journal of Physical Chemistry C, 2017. **121**(6): p. 3623-3631.
76. Che, S.N., et al., *The formation of cubic Pm(3)over-barn mesostructure by an epitaxial phase transformation from hexagonal p6mm mesophase.* Journal of the American Chemical Society, 2001. **123**(48): p. 12089-12090.
77. Landry, C.C., et al., *Phase transformations in mesostructured silica/surfactant composites. Mechanisms for change and applications to materials synthesist.* Chemistry of Materials, 2001. **13**(5): p. 1600-1608.
78. Liu, M.C., H.S. Sheu, and S.F. Cheng, *Drying induced phase transformation of mesoporous silica.* Chemical Communications, 2002(23): p. 2854-2855.
79. Quintard, P.E., et al., *Comparative lattice-dynamical study of the Raman spectra of monoclinic and tetragonal phases of zirconia and hafnia.* Journal of the American Ceramic Society, 2002. **85**(7): p. 1745-1749.
80. Zhao, X.Y. and D. Vanderbilt, *Phonons and lattice dielectric properties of zirconia.* Physical Review B, 2002. **65**(7).
81. Kaiser, W., P.H. Keck, and C.F. Lange, *Infrared Absorption and Oxygen Content in Silicon and Germanium.* Physical Review, 1956. **101**(4): p. 1264-1268.
82. Rigney, M.P., E.F. Funkenbusch, and P.W. Carr, *Physical and Chemical Characterization of Microporous Zirconia.* Journal of Chromatography, 1990. **499**: p. 291-304.
83. Ardizzone, S. and C.L. Bianchi, *Electrochemical features of zirconia polymorphs. The interplay between structure and surface OH species.* Journal of Electroanalytical Chemistry, 1999. **465**(2): p. 136-141.
84. Muhammad, S., et al., *Surface charge properties of zirconium dioxide.* Iranian Journal of Science and Technology Transaction a-Science, 2012. **36**(A4): p. 481-486.

85. Kujawa, J., S. Cerneaux, and W. Kujawski, *Removal of hazardous volatile organic compounds from water by vacuum pervaporation with hydrophobic ceramic membranes.* Journal of Membrane Science, 2015. **474**: p. 11-19.
86. Kujawa, J., et al., *Upgrading of zirconia membrane performance in removal of hazardous VOCs from water by surface functionalization.* Chemical Engineering Journal, 2019. **374**: p. 155-169.
87. Smith, A.L., *Vibrational Spectra and Assignments for Phenyl Chlorosilanes.* Spectrochimica Acta Part a-Molecular Spectroscopy, 1967. **A 23**(4): p. 1075-&.
88. Whiffen, D.H., *Vibrational Frequencies and Thermodynamic Properties of Fluoro-Benzene, Chloro-Benzene, Bromo-Benzene, and Iodo-Benzene.* Journal of the Chemical Society, 1956(Jun): p. 1350-1356.
89. Ho, Y.S., *Selection of optimum sorption isotherm.* Carbon, 2004. **42**(10): p. 2115-2116.
90. Atkins, P.W. and J. De Paula, *Atkins' Physical chemistry*. 8th ed. 2006, Oxford ; New York: Oxford University Press. xxx, 1064 p.
91. Freundlich, H., *Concerning adsorption in solutions.* Zeitschrift Fur Physikalische Chemie--Stochiometrie Und Verwandtschaftslehre, 1906. **57**(4): p. 385-470.
92. Langmuir, I., *The Adsorption of Gases on Plane Surfaces of Glass, Mica and Platinum.* Journal of the American Chemical Society, 1918. **40**: p. 1361-1403.
93. Bonilla-Petriciolet, A.n., D.I. Mendoza-Castillo, and H.E. Reynel-Ávila, *Adsorption Processes for Water Treatment and Purification*. 2017, Springer International Publishing : Imprint: Springer,: Cham. p. 1 online resource (XIV, 256 pages 57 illustrations, 19 illustrations in color.
94. El Qada, E.N., S.J. Allen, and G.M. Walker, *Adsorption of Methylene Blue onto activated carbon produced from steam activated bituminous coal: A study of equilibrium adsorption isotherm.* Chemical Engineering Journal, 2006. **124**(1-3): p. 103-110.
95. Hadi, M., et al., *Prediction of optimum adsorption isotherm: comparison of chi-square and Log-likelihood statistics.* Desalination and Water Treatment, 2012. **49**(1-3): p. 81-94.
96. Taniguchi, M. and J.S. Lindsey, *Database of Absorption and Fluorescence Spectra of > 300 Common Compounds for use in PhotochemCAD.* Photochemistry and Photobiology, 2018. **94**(2): p. 290-327.
97. Katritzky, A.R., *The Infrared Spectra of Heteroaromatic Compounds.* Quarterly Reviews, 1959. **13**(4): p. 353-373.
98. Ebadi, A., J.S.S. Mohammadzadeh, and A. Khudiev, *What is the correct form of BET isotherm for modeling liquid phase adsorption?* Adsorption-Journal of the International Adsorption Society, 2009. **15**(1): p. 65-73.
99. Tanabe, K., *Surface and Catalytic Properties of Zro2.* Materials Chemistry and Physics, 1985. **13**(3-4): p. 347-364.
100. Trudinger, U., G. Muller, and K.K. Unger, *Porous Zirconia and Titania as Packing Materials for High-Performance Liquid-Chromatography.* Journal of Chromatography, 1990. **535**(1-2): p. 111-125.
101. Sharma, M., J. Chawla, and G. Singh, *Cetyl trimethylammonium bromide as corrosion inhibitor for mild steel in acidic medium.* Indian Journal of Chemical Technology, 2009. **16**(4): p. 339-343.
102. Akay, G., et al., *Phosphate removal by red mud using crossflow microfiltration.* 1997 Jubilee Research Event, Vols 1 and 2, 1997: p. 1117-1120.
103. Oguz, E., A. Gurses, and M. Yalcin, *Removal of phosphate from waste waters by adsorption.* Water Air and Soil Pollution, 2003. **148**(1-4): p. 279-287.
104. Puckett, L.J., *Identifying the Major Sources of Nutrient Water-Pollution.* Environmental Science & Technology, 1995. **29**(9): p. A408-A414.
105. Zhao, D.Y. and A.K. Sengupta, *Ultimate removal of phosphate from wastewater using a new class of polymeric ion exchangers.* Water Research, 1998. **32**(5): p. 1613-1625.
106. Liu, H.L., et al., *Removal of phosphate by mesoporous ZrO2.* Journal of Hazardous Materials, 2008. **151**(2-3): p. 616-622.

107. Klahn, M., et al., *IR spectra of phosphate ions in aqueous solution: Predictions of a DFT/MM approach compared with observations.* Journal of Physical Chemistry A, 2004. **108**(29): p. 6186-6194.
108. Socrates, G. and G. Socrates, *Infrared and Raman characteristic group frequencies : tables and charts*. 3rd ed. 2001, Chichester ; New York: Wiley. xv, 347 p.
109. Gorce, J.P., et al., *Infrared active methyl group vibrations in tetratetracontane: A probe for chain end organization and crystal structure.* Journal of Physical Chemistry B, 2004. **108**(10): p. 3130-3139.
110. Ulman, A., *An introduction to ultrathin organic films: From Langmuir-Blodgett to self-assembly*. 1991, Boston: Academic Press.
111. Suecker, I., *[Dissolution of Difficult to Disolve Phosphate by Acids and Complex-Forming Agents].* Urologe, 1964. **3**: p. 218-22.